Structural Basis of Kinesin-1 Autoinhibition and Its Control of Microtubule-Based Motility

Md Ashaduzzaman[1], Richard J. Mckenney[1], Jawdat Al-Bassam[1]†

Department of Molecular Cellular Biology, University of California, Davis, California USA

Abstract

Kinesin-1 is the first identified microtubule-based motor protein that drives anterograde intracellular transport of diverse cargoes in eukaryotic cells. Defects in kinesin-1 activity have been implicated in various human neurological disorders and intracellular pathogens such as bacteria and viruses hijack its activity. Despite its importance, the molecular mechanisms governing kinesin-1 activation remains poorly understood. Here, we report an 8.0-Å cryo-electron microscopy structure of the kinesin-1 heterotetramer composed of two kinesin heavy chains (KHC) and two light chains (KLC), in its autoinhibited conformation. Our structure reveals a complex 36-nm head-to-tail assembly in which self-folded dimeric KHCs are stabilized by asymmetrically arranged KLCs through a combination of intramolecular and intermolecular interactions. This state inhibits kinesin motility by constraining the dimeric motor domains in a configuration that is incompatible with motility. Notably, our structure also shows that the dimeric KLC TPR cargo-binding domains are occluded, providing a structural basis for the autoinhibition of both motor activity and cargo binding. Functional studies along with structural modeling suggest that binding of known regulatory factors, such as MAP7D3, to the KHC coiled coils likely competes with intramolecular coiled-coil interactions, resulting in the unfurling of the autoinhibited structure and activation of motor activity. Our findings provide a molecular framework for understanding the regulation of kinesin-1 activity and its implications for intracellular transport.

† Correspondence contact: jmalbassam@ucdavis.edu

Keywords: cryo-EM, structure, kinesin, kinesin-1, KIF5b, motor protein, plus-end directed, microtubule motor.

Introduction

Kinesin-1 (KIF5B, hereafter “kinesin”) is the founding member of a superfamily of motor proteins essential for intracellular transport along microtubules[1,2]. As the cell's most ubiquitous anterograde motor, it transports a diverse range of cargoes toward the microtubule plus-end[3-6]. While its processive, hand-over-hand motility mechanism is well-understood from studies of truncated constructs[7,8], how the full-length motor is precisely regulated remains a central question. In cells, kinesin-1 exists as a heterotetramer of two kinesin heavy chains (KHCs) and two kinesin light chains (KLCs). This complex folds into a compact, autoinhibited conformation, a state first inferred from hydrodynamic studies showing the native particle is roughly half the length of the motile motor[9-11]. More recently, low-resolution structures from negative stain electron microscopy and cross-linking mass spectrometry (XLMS) visualized this "lambda particle" shape[12-14]. Despite these advances, the precise placement of individual KHC and KLC domains within this assembly has been unknown.

Beyond suppressing motility, this inactive state must also control cargo engagement. Kinesin binds a vast array of cargoes through two main hubs: the KLC tetratricopeptide repeat (TPR) domains, which recruit adaptors via conserved peptide motifs[15,16], and the KHC stalk/tail, which interacts with adaptors like TRAK and JIP1/3[17-19]. For proper regulation, these cargo-binding sites must be inaccessible in the inhibited state to prevent premature loading. Yet, it has remained unclear how the KLC TPR domains are natively configured within the autoinhibited complex and how their availability is regulated.

Decades of research have provided key but sometimes paradoxical clues about the activation mechanism. The KHC C-terminal tail, containing a conserved IAK motif, is a potent inhibitor of motor activity[13,20,21]. However, while its deletion produces a constitutively active motor, mutation of the IAK motif alone is insufficient to fully activate processivity in the full-length complex[12,22]. This suggests other factors are required, a role now largely attributed to cargo adapter proteins that bind to the KLCs[16,22], and MAP7 family proteins[22-24]. MAP7 proteins dramatically enhance kinesin's microtubule association and are required for its activity in cells[44–48]. This has led to a model of sequential activation, where MAP7 first recruits and activates the motor, which in turn unmasks the KLCs for cargo binding[25]. While this model explains many observations, the structural basis for this sequence—how the complex physically unfurls to release both motor and cargo inhibition—has been a complete mystery.

To resolve this, we determined an ~8.0-Å cryo-EM structure of the autoinhibited human kinesin-1 heterotetramer. Our structure reveals a striking asymmetry in how the KLCs organize the complex. One KLC TPR domain acts as a clamp, stabilizing the folded KHC coiled-coils, while the other acts as a wedge, locking the motor domains in a non-motile state. Furthermore, we uncover a novel mechanism of cargo-binding autoinhibition, where C-terminal KLC helices fold back to sterically block the cargo-binding groove of the TPR domains. Together, these findings provide a comprehensive structural blueprint for how kinesin-1 co-regulates its motor and cargo-binding functions, establishing a physical framework for its sequential activation.

Results

Cryo-EM structure of kinesin in the autoinhibited state

A recombinant human kinesin heterotetramer (KIF5B-mScarlet and KLC1) was purified as previously described[22]. The resulting kinesin lambda particle[13] was stabilized with GraFix[26] and

vitrified to obtain intact particles (**Figure S1**). Cryo-EM data was collected in thick ice, which limited the attainable resolution. To improve the map, we refined single particle structures by dividing the assembly into four sub-regions with resolutions ranging from 5.6 to 8.6 Å (see Materials and Methods; **Figures S2-S7**). The final merged electron density map revealed clear secondary structure, enabling us to model the assembled KHC and KLC helical, coiled-coil, and folded domains in their heterotetrametric organization, excepting ~20 residues at the KLC N-termini (**Figure S8; Figure 1A-B**).

The KHC coiled-coils folds back at the "elbow"[13] -forming the lambda particle[13] bringing the KHC motor domains in proximity to the KHC C-terminal tails (**Figure 1A-B**). The KHC and KLC helical, coiled-coils, globular motor and TPR domains matched their previously determined or AlphaFold predicted structures[12,13,16] (**Figure S9**), but the structure revealed their intra- and inter-molecular interactions. The dimeric KHC consists of N-terminal motor domains (motor-A and motor-B), followed by a series of coiled-coil segments: CC0, $CC1^{KHC}$, $CC2^{KHC}$, CC3, and CC4. These are followed by two C-terminal KHC tail regions, each fused to a well-ordered mScarlet fluorescent protein (mScar) through a short linker (**Figure 1A-B; Figure 2A**). The dimeric KLCs consist of two N-terminal KHC-binding KLC coiled-coil regions, $CC1^{KLC}$ and $CC2^{KLC}$ followed by a linker-helical region (L-H), and a cargo binding TPR domain. Following the TPR domains, the KLC C-terminal regions—H1, H2, Self cargo (SC), and H3, which were all previously not observed, are all well-ordered (**Figure 2A)**.

A structural model for autoinhibition of motor activity via extensive intramolecular self-folding

The overall structure reveals an extended, 36-nm comet-shaped particle formed by the kinesin heavy chain (KHC) dimer folding back on itself (**Figure 1**). This lambda-shaped fold is defined by a "forward" arm (CC0, CC1, CC2) and a "return" arm (CC3, CC4), connected by a novel U-shaped structure that composes the elbow[13]and facilitates the turnaround after $CC2^{KHC}$ (**Figure 2**). This anti-parallel arrangement holds the N-terminal motor domains in an orientation incompatible with microtubule binding, providing a direct structural explanation for autoinhibition. The entire KHC assembly is further stabilized by the asymmetrically folded kinesin light chains (KLCs).

Several critical interactions lock the motor domains into this inhibited conformation. The neck coiled-coil (CC0) forms a dimer that packs between the two motor domains as a four-helix bundle, orienting them perpendicular to the particle's long axis (**Figure 1C-D; Figure 2A-B**). This state is further stabilized by the KHC C-terminal tails (tail-A and -B), which emerge from the CC4 return arm to interact with only one of the motor domains (motor-A). This asymmetric 2:1 tail-to-motor interaction is consistent with biochemical findings[51] but is structurally distinct from contacts observed in prior models of isolated KHC fragments or MT-bound complexes[27,28]. Finally, a previously designated 'hinge' region[29,30] at the junction of $CC1^{KHC}$ and $CC2^{KHC}$ is in good agreement with recent computational models and negative stain EM data[12,13], validating another key feature of the fold.

The structure revealed a surprisingly asymmetric organization of the dimeric KLC subunits. $CC1^{KLC}$ folds around each KHC CC3-CC4 in anti-parallel manner leading to $CC2^{KLC}$ which is parallel to CC3-CC4 (**Figure 3E**). The N-termini of the $CC2^{KLC}$ helices form a tetrameric parallel coiled-coil structure with KHC CC3-CC4, resulting in the dimerization of the KLCs with the KHCs (**Figure 3E, left middle pane**l). This produces a parallel eight helical bundle sandwiched between

CC1^{KHC}-and CC4 (**Figure 3E**). Following the tetrameric KHC-KLC assembly zone, the remaining CC2^{KLC} 90-residues forms a homo-dimeric coiled-coil, which leads to two linker-helices (L-H-A, L-H-B) (**Figure 3F-G**), revealing that the KLCs homodimerize in this region. Although, L-H -A and L-H -B regions emerge from the symmetric CC2^{KLC} dimer, they fold in opposite directions toward the asymmetrically positioned KLC-TPRs (**Figure 3C, F-G**). KLC-TPR-A bridges alongside the two KHC-KLC coiled-coil arms stabilizing the autoinhibited structure (**Figure 1-2**, **Figure 3G**), while KLC TPR-B wedges between the two motor domains and closely interacts with motor-B (**Figure 1-2; Figure 3A, C**). The total buried surface area by KHC-KLC interaction is about 5500 Å and represent mostly coiled-coiled interactions (**Figure S9**).

Our cryo-EM structure of autoinhibited kinesin reveals significant departures from previous models generated by AlphaFold or from negative stain EM data[12] (**Figure S10**). Key differences include the overall organization of the KHC coiled-coils, the binding interfaces of the KLC TPR domains, and the orientation of the motor domains. Notably, while the general position of the elbow is consistent with that reported by Tan et al.[12], its structure is fundamentally different. Instead of a sharp turn predicted by AlphaFold, our structure reveals a broad, U-shaped bend spanning ~40 residues (Glu640-Glu686) that guides the KHC back upon itself. Furthermore, our model provides the first complete structural view of the neck coiled-coil (CC0) and the C-terminal tails in the autoinhibited context, clarifying their crucial roles in stabilizing the complex and regulating activation.

To validate our model against independent experimental data, we re-analyzed published cross-linking mass spectrometry (XLMS) datasets from Tan et al.[12]. We found that these cross-links, which map interactions within KIF5B/KIF5C and KLC1, show remarkable consistency with the domain contacts observed in our cryo-EM structure (**Supplementary Text, Figures S12-S14**). Crucially, our model provides a clear structural rationale for numerous cross-links between domains that were previously unexplainable with models derived from negative stain EM or AlphaFold[12] (**Figure S10**). This high degree of consistency with existing biochemical data provides strong validation for the novel architectural features revealed in our structure. A detailed comparison of the XLMS data to our model is provided in the Supplementary Text.

Dimeric KHC C-terminal tails bind to one motor domain in the autoinhibited state

The KHC C-terminal tails, which are crucial for forming the autoinhibited state[31,12,13], are revealed in our structure to be ordered, W-shaped helical domains (**Figure 2; Figure 3A, D**). Emerging from CC4, these tails interact with the motor domains in a strikingly asymmetric fashion. Only one tail (tail-A) directly engages a single motor domain (motor-A), binding near its α2 and α3 helices with the conserved IAK motif positioned at the junction of CC4 and the first tail helix (**Figure 3A, D**). The second tail (tail-B) remains unbound to a motor. This asymmetry is further evidenced by the staggered positions of the C-terminal mScar tags: the tag on the bound tail-A is positioned ~10 Å lower than the tag on the unbound tail-B, suggesting that binding to motor-A constrains and tightens the tail-A structure (**Figure 1-2**).

This model of the tail-motor interaction differs significantly from previous structures derived from co-crystals of isolated tail peptides or from cryo-EM maps of MT-bound constructs[27,28]. Our structure of the full-length, autoinhibited complex demonstrates that the native inhibitory contact is critically dependent on structural context—specifically, the dimerization and orientation of the tails by the CC4 coiled-coil. This architecture positions the

tails correctly for their inhibitory function. Furthermore, these core tail-motor interactions are likely preserved even in the absence of KLCs, as suggested by previous negative stain EM studies on KHC dimers[24], highlighting this as a fundamental feature of KHC autoinhibition.

Asymmetric KLC TPR domains bind the self-folded KHC coiled-coils and a single motor domain

Despite recent insights into autoinhibited kinesin[12,13], the precise positioning of the KLC TPR domains has remained an unresolved question. Our structure resolves this by revealing that the two KLC-TPR domains bind in a surprisingly asymmetric manner to the symmetric KHC dimer (**Figure 1D, Figure 2, Figure 3A-E**). Instead of engaging equivalent sites, each TPR domain binds to a distinct region of the KHC, adopting a unique role. One TPR domain (TPR-A) acts as a structural clamp, bridging across the KHC coiled-coils, while the other (TPR-B) functions as a wedge, inserting between the motor domains.

TPR-A stabilizes the folded KHC architecture by bridging the $CC1^{KHC}$-$CC2^{KHC}$ and CC3-CC4 arms. It uses its narrow surface, composed of inter-helical repeat turns, to clamp the KHC coiled-coils together in their folded conformation (**Figure 1-2; Figure 3D**). This interaction is critical for maintaining the overall integrity of the lambda-shaped particle. In contrast, TPR-B is positioned as a triangular wedge between the two KHC motor domains, on the side opposite the dimerized CC0. It interacts closely with one motor domain (motor-B), using the helices of its TPR repeats 2-5 to lock the motors in their inhibited state (**Figure 3A-D**). The amino acid sequences at these unique KLC-KHC interaction interfaces are highly conserved across species (**Figure S11E, G**), underscoring their functional importance.

Beyond stabilizing the KHC fold, our structure reveals a mechanism for KLC self-inhibition. In both KLC subunits, ordered C-terminal helical regions—H1, H2, and a self-cargo (SC) motif—fold back to occupy the concave, cargo-binding face of their respective TPR domains, sterically preventing adapter protein engagement (**Figure 2**). This complex, asymmetric arrangement is accommodated by distinct conformations of the KLC linker helices (L-H and H3). For example, the linker following TPR-A (H3-A) binds along $CC1^{KHC}$, while the linker following TPR-B (H3-B) binds across the top of motor-B (**Figure 3A-D**). Our work provides the first complete view of all KLC helical segments within the context of the fully autoinhibited kinesin structure (**Figure 3F**).

The KLC TPRs are autoinhibited by C-terminal helical sequences.

Previous studies proposed that KLC is autoinhibited via an N-terminal 'LFP' sequence that competes with cargo proteins for binding to the TPR domain[32,33]. Our structure confirms that the KLC TPRs exist in an autoinhibited state but reveals a fundamentally different mechanism driven by C-terminal elements. We find that the concave cargo-binding groove of each TPR domain is occupied by a series of helices (H1, H2, and a self-cargo [SC] motif) that are C-terminal to the TPR domain itself (**Figure 2; Figure 4A-C**). H1 acts as a connector that folds back from the TPR domain, positioning H2 and the SC motif to sterically block the interface for Y- or W-acidic cargo motifs (**Figure 4B-D**). This self-inhibited state is further locked in place by the most C-terminal helix, H3, which anchors the KLC to adjacent KHC domains ($CC1^{KHC}$ or motor-B). A subtle difference seen between two KLC TPRs is H1-A is more bent toward the concave face of TPR-A than H1-B (**Figure 4B-C**).

Thus, our work provides the first structural view of KLC autoinhibition within the intact kinesin complex, demonstrating that both TPR domains are blocked by C-terminal intramolecular interactions. This finding directly contrasts with the previously proposed N-terminal 'LFP' mechanism[32]. We attribute this discrepancy to the different experimental contexts: our structure represents the full-length heterotetramer, whereas earlier studies utilized isolated KLC proteins with truncated C-termini that lacked the inhibitory helices we observe here[32]. The context of the full complex is therefore essential for revealing the mechanism of KLC autoinhibition.

Restriction of the motor domains in the autoinhibited structure

While it is known that full-length kinesin motility is strongly repressed[22,29], the precise structural mechanism has been unclear. Our structure reveals that the dimeric motor domains are locked into a tightly constrained, non-processive configuration through a multi-point locking mechanism (**Figure 5A-B**). This is achieved by specific interactions with the KHC C-terminal tail (tail-A), a KLC TPR domain (TPR-B), and the neck coiled-coil (CC0). Tail-A binds directly to motor-A, while TPR-B acts as a wedge between the two motors, tightly engaging motor-B. Simultaneously, the CC0 dimer is packed into a unique conformation that further restricts the motors' positions (**Figure 3A-B; Figure 5A-B**).

To understand the functional consequences of this locked arrangement, we compared it to motile or unbound kinesin structures, including the MT-bound KIF1A dimer and the free rat kinesin motor dimer crystal structure[34,35]. This comparison reveals a dramatic reorientation: one of the motor domains in our autoinhibited structure is twisted by 120°-140° around its neck linker junction relative to its position in the motile states (**Figure 5C-F**). As a direct result, the microtubule-binding interfaces (the α4 helices) of the two motors are severely misaligned and cannot engage a microtubule simultaneously (**Figure 5E-F**). Therefore, our structure demonstrates that autoinhibition physically prevents processive motility by locking the motors in a conformation where the hand-over-hand stepping mechanism is impossible.

Map7D3 binding to $CC1^{KHC}$ destabilizes the autoinhibited state

MAP7 family proteins are critical for kinesin function in vivo[23,36]. While it is established that MAP7 enhances kinesin's microtubule (MT) association, its direct role in activating motility has been ambiguous[23]. Some studies suggest full activation requires a cargo-adapter protein[22], while others observed increased motility that could be attributed to a higher MT landing rate rather than true activation[23,24]. More recently, the paralog MAP7D3, which binds kinesin more tightly, was shown to enhance motility even in truncated K560 constructs, suggesting a more direct activation mechanism[43].

To investigate how MAP7D3 activates kinesin, we first used AlphaFold3 to model the interaction between the MAP7D3 C-terminal domain ($MAP7D3^{CT}$) and the KHC[30,37,38]. The model predicted that $MAP7D3^{CT}$ forms a four-helix bundle with the $CC1^{KHC}$ region, an interaction that would sterically clash with the autoinhibited fold and disrupt critical stabilizing contacts (**Figure S14, Figure 6A**). To test this hypothesis, we a performed single-molecule TIRF microscopy assay. As expected, the kinesin heterotetramer was strongly autoinhibited in the absence of MAP7D3CT[22-24,36]. In stark contrast, the addition of $MAP7D3^{CT}$ triggered a ~12-fold increase in the number of processive runs (**Figure 6B-C**). These results provide direct functional validation for

our structural model, demonstrating that MAP7D3 binding is sufficient to break the autoinhibited state and activate processive motility.

This activation mechanism also explains how MAP7D3 enhances cargo binding, as shown in previous work[25]. Our model suggests this occurs because disrupting the autoinhibited complex liberates the KLC TPR domains from their sequestered positions, increasing the accessibility of their cargo-binding sites. Therefore, MAP7D3 functions as a dual-action activator: it sterically disrupts the autoinhibitory interface to directly trigger motility, which in turn unmasks the KLCs to promote the recruitment of cargo adapters (**Figure 6D**).

Discussion

For decades, research on kinesin-1 has defined its hand-over-hand motility mechanism[3,21,39], yet the molecular basis of its spatiotemporal regulation has remained poorly understood. It is well established that the kinesin heterotetramer is autoinhibited via intramolecular interactions[29,31,40], but a complete structural picture of this state has been missing. Recent work has converged on a model of sequential activation, where factors like MAP7 first activate motility, which in turn permits the loading of cargo via the KLC TPR domains[22-25,36]. However, the structural basis for this coordinated process—how the motor is inhibited from both moving and binding cargo, and how activators could reverse this—has been a central unresolved question.

Our cryo-EM structure of the fully-inhibited kinesin provides a direct answer. We show that the complex is a precisely organized assembly where long-range interactions create a dual-locked state. First, motor activity is suppressed by a network of asymmetric contacts: the KLC TPRs act as structural clamps and wedges, while the KHC C-terminal tails tether the motor domains in a non-processive conformation (**Figures 1-3; Figure 5**). Second, and unexpectedly, cargo binding is independently blocked by a C-terminal KLC segment that occupies the TPR cargo-binding groove, a mechanism fundamentally different from previously proposed models (**Figure 4**). This dual-inhibition architecture provides a comprehensive blueprint for how kinesin maintains a robustly 'off' state, while also revealing distinct structural points of regulation that can be targeted by activators to sequentially unlock motility and cargo loading.

A structure-based model for kinesin activation and the sequential loading of cargo

Our structural and biochemical data converge on a comprehensive model for the sequential activation of kinesin, integrating MAP7-mediated recruitment with the relief of both motility and cargo-binding autoinhibition **(Figure 6)**. The cascade begins when MT-bound MAP7D3 recruits an autoinhibited kinesin, increasing its local concentration on the microtubule **(Figure 6D, I)**. The MAP7D3 C-terminus then binds to CC1KHC, creating a direct steric clash that, as predicted by our modeling **(Figure S14; Figure 6A)**, destabilizes the compact autoinhibited fold **(Figure 6D, I-II)**.

This initial disruption triggers a large-scale conformational rearrangement. The complex unfurls, nearly doubling in length from ~36 nm to ~72 nm, which releases inhibitory constraints on the motor domains—including the unravelling of the CC0 neck coiled-coil **(Figure 6D, III-IV, middle panels)**—to permit hand-over-hand motility. Concurrently, this global unfolding liberates the KLCs, causing the C-terminal inhibitory helix to dissociate from the TPR cargo-binding groove.

This final step unmasks the cargo-binding sites, rendering the now-motile kinesin fully competent for cargo-adapter engagement **(Figure 6D, III-IV, top panel)**.

Conclusion

Elucidating the intramolecular interactions that govern kinesin-1 autoinhibition has been a long-standing challenge in the motor field. Our work provides a direct structural answer, revealing a comprehensive blueprint for how motor activity and cargo engagement are co-regulated. By demonstrating how a network of asymmetric, long-range interactions creates a dual-locked state, this model establishes a clear foundation for future mutational studies to dissect these mechanisms in vitro and in vivo. Furthermore, it provides a powerful framework for exploring autoregulation across the entire kinesin superfamily.

Acknowledgement:

We thank Dr Michael Cianfrocco (University of Michigan, Ann Arbor) for early support, advice in early stages and encouragement throughout the project. We thank Dr. Kyoko Chiba (Tohoku University) for the generation of kinesin reagents and Dr. Kyoko Okada for advice and experimental support. We thank Dr Camille Scott and the UC-Davis High performance computing core facility (HPCCF) for computational support. We would like to thank the Dr Ed Eng, Dr Eugene Chua at the NIH National center for cryo-electron microscopy access and training (NCCAT) for providing advice and help with sample preparation and for initial data collection. Large scale Cryo-EM data were collected at NCCAT and the Simons Electron Microscopy Center located at the New York Structural Biology Center, supported by the NIH Common Fund Transformative High Resolution Cryo-Electron Microscopy program (U24 GM129539, and NIGMS R24 GM154192) and by grants from the Simons Foundation (SF349247) and NY State Assembly. JAB and RJM are supported by the NIH (R01GM110283 to JAB and R35GM124889 to RJM). The kinesin cryo-EM map and model coordinates were submitted to the EMDB and PDB with the following accession numbers (XXXXX, XXXXX).

Materials and Methods

Cryo-EM sample preparation and data collection

Kif5B-mScarlet-KLC1 at 1 mg/mL was tested for crosslinking with 0.01-0.08% (v/v) glutaraldehyde at room temperature for 30 minutes and analyzed on SDS-PAGE gel to find optimal crosslinking concentration. The sample was prepared for cryo-EM sample with 0.06% (v/v) glutaraldehyde with GraFix[26] system using 20 mM HEPES pH 7.2, 100 mM KCl, 1 mM $MgCl_2$, 5 mM B-ME, 1 mM EGTA and loaded onto 10-40% (v/v) sucrose gradient with 1 mg/mL Kif5B/KLC1 and ran for 16 hours at 4 C at 40000 rpm (**Figure S1A**). Sample was manually collected with a pump at 10s interval of ~200 µL. Fractions containing Kif5B/KLC1 was then neutralized with 1 mM Tris-HCl pH 7. Crosslinked samples were dialyzed to remove sucrose with 20KDa MWCO Amicon filters and concentrated with 100 KDa MWCO centrifugal filter. The crosslinked samples were analyzed for their average masses using a Refeyn Mass Photometer (Refeyn Ltd.) revealing a mass consistent with pure heterotetramers (**Figure S1B**). Quantifoil R1.2/1.3, 300 mesh Au grids were plasma cleaned with H2/O2, 50 W, for 30 sec and Vitrobot blotting conditions were set at 4°C and 100% humidity. Kif5B/KLC1 sample with detergent FOM (0.12x-1x CMC) (VitroEase™, Thermo-Fisher) at 3 mg/mL was pipetted to the grids and blotted 3-3.5s and plunge-freeze in liquid ethane.

For Cryo-EM datasets collection, G2 Krios microscope (ThermoFisher) at 300 kV equipped with Falcon IV detector (ThermoFisher) at 130,000x magnification was set and data acquisition was done using Leginon[41] beam-image shift[42] with 7s exposure with total dose of ~48 e-/Å at pixel size 0.926 Å with defocus -0.8 µm to -2.5 µm at 130,000x magnification and filtered through a Selectris 20 eV energy filter. Total four datasets of 55674 movies were saved as Electron-event-representation (EER)[43] files at image dimensions of 4096x4096 pixel.

Cryo-EM structure determination

Each EER-Movie dataset was imported into RELION[44] separately and Motion-corrected with EER fractionation of 32 using RELION's own implementation with B-factor of 150 and patches of 5x5 with no binning. CTF estimation was done using CTFFIND-4.1[45]. Initial picking was done using Laplacian -of-Gaussian (LoG) in RELION with 100x450 diameter and extracted in 200-pixel box at 3.704 Å/pixel. Multiple 2D-, 3D-classification and 3D-refinement steps helped to remove junk, broken or open kinesin particles leading to 36-nm comet-shaped 'lambda' particle structures from each of the datasets in which the particle has a wide globular organization at one end and an elongated narrow region at the other end. Iterative, 2D-classifications were done in cryoSPARC[46] and particles were re-extracted in RELION[44] and re-classified in cryoSPARC[46] and ~4 millions particles were re-picked with Topaz[47] in RELION[44]. To accurately center these elongated 'lambda' particles, we used an iterative strategy of picking particles followed by T=0 classification[48] (**Figure S1, Figure S2-S4**). These particles were better aligned with single class 3D classification using T=0[48] using a Kinesin-1 (Tan et al 2023[12]) negative stain low resolution map. Aligned particles were iteratively refined, classified, and polished (**Figure S3**) to accumulate 664938 particles extracted to 1.852 Å/pixel. Global consensus 3D-refined structures were determined using iterative 3D-refinement and 3D-classification in large box formats (**Figure S5)**. Density for the sub-regions of the consensus cryo-EM map were further improved by re-centering, re-extraction, and local refinement leading to 5.6-8.0 Å resolution (**Figure S5-S6**). Re-centering and re-extraction into 150-pixel box with 1.852 Å/pixel followed by local refinement

used for TPR's and part of CC1 and CC4 and KLC-CCs with 5959495 particles. 3D-classification without alignment shows single class with 103108 particles with both Motor in closed conformation which were then 3DFlex[49] and local refined in cryoSPARC[46] to solve the Motor-Tail with mscarlets-KLC (TPR-B and the C-terminal residues). These refined subregion maps were combined by overlaying onto the consensus map, leading to full kinesin 'lambda'' particle density map to 5.6-8.0 Å resolution throughout the structure. Model placed map using EMAN from SBGrid software packages[50] was used to align the CC2-CC3 turnaround followed by 3D variability analysis separated 30746 particles which was local refined at 300 pixel box at 1.852 Å/pixel. Local resolutions were estimated using PHENIX[51]. We carried out *de novo* model building for all the α-helical regions of the KHC and KLC including all CC regions, kinesin motor, and KLC TPR domains (**Figure S7**). Cryo-EM data collection, single particle data processing, and final model statistics are shown **Table I.**

Model building and XLMS data visualization

Local refined maps were aligned and a ChimeraX[52] vop map was created for full-length Kinesin-1 heterotetramer (**Figure S7**). AlphaFold3 predicted KIF5B-KLC1 local fold was used to placed motors, CCs, TPRs and mscarlets (**Figure S8**). The CC0 dimer, $CC2^{KHC}$-CC3 turn-around and C-terminal tail of KHCs and KLCs were modeled manually. All placed models were real space refined in PHENIX and validated using MolProbity[51,53]. KIF5C/KLC1 model was manually built to plot XLMS data from Tan et al.[12] using XMAS[54]. KIF5B/KLC1 and KIF5B dimer XLMS data was similarly plotted for visualization from Tan et al.[12].

AlphaFold3 model predictions

To determine kinesin models, sequences for two copies of the KIF5B and KLC1 and two ATP and Mg molecules were entered into a single multi-subunit determination using the AlphaFold3 server (www.alphafoldserver.com)[38]. Values of moderate to high confidence pIDDT values per residue displayed (**Figure S10B**) and their corresponding PAE matrix with accuracy of residue position error. To determine KIF5B-MAP7D3-CT AlphaFold3 models, sequences for two copies of KIF5B (residues 1-587) $MAP7D3^{CT}$ (residues 476-876) were entered into a single multi-subunit determination using the AlphaFold3 server. A single representative model is presented in **Figure S14A** with the moderate to high confidence pIDDT values per residue displayed.

TIRF assays

TIRF flow chambers were assembled from acid-washed glass coverslips (prepared as described in [Citation]), pre-cleaned slides (ThermoFisher), and double-sided tape. Chambers were functionalized by sequential incubation with 0.5 mg/ml PLL-PEG-biotin (Surface Solutions) for 5–10 min and 0.5 mg/ml streptavidin (ThermoFisher) for 5 min.

Taxol-stabilized microtubules (10 µM) in BRB80 buffer (80 mM PIPES pH 6.8, 1 mM $MgCl_2$, 1 mM EGTA) were flowed into the chamber and incubated for 2–5 min to allow immobilization. Unbound microtubules were removed by washing with SRP90 assay buffer (90 mM HEPES, 50 mM KCH_3COO, 2 mM $Mg(CH_3COO)_2$, 1 mM EGTA, 10% glycerol, pH 7.6) supplemented with 1 mg/ml BSA, 0.05 mg/ml biotin-BSA, 0.2 mg/ml K-casein, 0.5% Pluronic F-127, 10 µM taxol, and 1 µM phalloidin. Finally, Kinesin-1 (KIF5B-KLC1) at the indicated concentrations, with or without MAP7D3 CT, was introduced in SRP90 assay buffer containing 2 mM Mg-ATP (Sigma).

All imaging was performed on a Nikon TE microscope equipped with a PlanApo 100×/1.49 NA objective, a TIRF illuminator (LU-N4), and an Andor iXon EMCCD camera, controlled with MicroManager 1.4 Software[55]). Data were analyzed manually using kymographs generated in ImageJ (Fiji).

Figure legends

Figure 1: Cryo-EM structure of the autoinhibited kinesin KIF5B-KLC1 reveals the organization of the hetero-tetramer and the asymmetric subunit interactions in the lambda particle.

A) Two 90° rotated views of a segmented kinesin KIF5B-KLC1 heterotetrametric Cryo-EM map. The KHC subunits, KHC-A and -B, are colored blue and cyan, while the KLC subunits, KLC-A and -B, are colored red and salmon. Densities for the mScarlet (mScar) proteins fused on the KHC C-termini are colored purple.
B) Two 90° rotated views of the modeled and segmented transparent kinesin KIF5B-KLC1 heterotetramer cryo-EM map, colored as shown in A.
C) Two 180° rotated views of the modeled and segmented KIF5B-KLC1 heterotetramer Cryo-EM map showing the asymmetric KLC-TPR interactions with KHC subunits without the mScarlet densities.
D) A dissociated view showing the isolated KLC-A, KLC-B and KHC-A, KHC-B dimeric subunits matching the orientation of left panel in C.

Figure 2: The organization of the KHC and KLC domains in the kinesin lambda autoinhibited structure.

C) Linear detailed domain organization of the human KIF5B and KLC1 are shown. KIF5B (KHC) domains include the motor domain, neck linker, CC0, $CC1^{KHC}$, $CC2^{KHC}$, CC3, CC4 and tails. The mScarlet (mScar) fused onto the C-terminus is shown. The KLC1 (KLC) includes: $CC1^{KLC}$, $CC2^{KLC}$, L-H, TPR, H1, H2, Self-cargo (SC), H3. Boundaries are indicated in residue numbers, below, and each are colored to match colors for their models shown in B and C.
D) The kinesin-1 KIF5B-KLC1 heterotetramer model in domain colors shown in panel A. KLC-TPR-A and -B are shown in red and dark red, respectively.
E) 180° rotated view of panel (B) is shown.

Figure 3: Close up domain interactions in the Kinesin lambda autoinhibited structure: Close up views of interactions of the domains with coloring scheme shown in Figure 2. Each view is shown with a top left inset showing the orientation of the view

A) Bottom view of the KHC motor-A, -B, tail-A, B and the KLC-TPR-B
B) Side view showing the KHC dimeric motor-A, B domains and the packed CC0 and $CC1^{KHC}$ domains
C) Side view showing the KHC motor-B interacting with KLC-TPR-B and the self-folded state of $CC1^{KHC}$ and CC4.
D) Side view showing the KHC motor-A interacting asymmetrically with tail-A and tail-B which emerge from CC4. The IAK motifs, labeled with arrows, lie at the end of CC4.

E) A side view of the fully folded coiled-coil regions of kinesin including $CC1^{KHC}$, $CC2^{KHC}$, CC3, CC4, $CC1^{KLC}$, $CC2^{KLC}$ and H3. The KHC-CC N- and C-termini are labeled.
F) Top-tilted view showing the KLC-TPR-A bound to the two KHC halves stabilizing CC1 folding onto CC4
G) A side view of the structure, with CC4 being faded, showing the $CC1^{KLC}$ and two directions of the L-H-A, -B extending toward the KLC-TPR-A and TPR-B

Figure 4: **The topology and self-regulation of the KLC subunits in lambda kinesin autoinhibited structure**

A) A general view of the kinesin structure with KHC shown in faded white while KLC is shown in rainbow colors denoting the N- to C-terminal topology in a Rainbow gradient from blue to red colors, respectively. Each TPR domain is shown and its orientation transformed via arrows to orient them in a comparable manner. The top left isolated KLC-TPR models show the role of the KLC C-terminal helical regions, colored in gold, autoinhibiting access to the cargo binding concave surface of the TPR domains.
B) A view of the KLC-TPR-B domain with the helical regions of the TPR fold shown in surface representation with the KLC-C-terminal helical regions shown in ribbon form.
C) A view of the KLC-TPR-A domain in the same orientation described in B
D) A view of the KLC-TPR structure with the Y-acidic motif cargo peptide bound to the concave surface of the KLC-TPR[16].
E) An overlay of the KLC-TPR structure (brown and salmon) in two states described here and the free (cyan) and Y-acidic motif cargo-peptide bound form (blue) overlaid. The SC and H2 in autoinhibit the TPR domain and sterically hinder cargo peptide binding.

Figure 5: **The kinesin motor domains are restricted from motility by the lambda autoinhibited kinesin structure interactions**

A,B) two views of the Kinesin structure showing the KHC motor A, B (blue) bound by the KHC tail-A, -B (orange and gold) and the KLC-TPR domain (red) and CC0 (cyan) is packed beneath $CC1^{KHC}$. The MT binding site of each motor domain is highlighted with α4 helix shown in yellow.

C) A view matching the orientation shown in panel A of the dimeric kinesin motor domain crystal structure[34] (PDB ID: 3KIN) showing the motor domains (magenta) and the CC0 (cyan). The MT binding site of the motor domain MT is highlighted with α4 helix shown in yellow.
D) A view matching the orientation shown in panel A of the dimeric KIF1A motor domain cryo-EM model along the MT protofilament[35] (PDB ID:8UTN) showing the motor domains (magenta) and the CC0 (cyan). The MT binding site of the motor domain is engaged with the MT and this binding site is highlighted with α4 helix shown in yellow.
E) Overlay of view of the CC0, Motor-A and -B domains shown in A with those shown in C.
F) Overlay of view of the CC0, Motor-A and -B domains shown in B with those shown in D.

Figure 6: MAP7D3 binds KHC-CC1, sterically competing with the autoinhibited kinesin conformation, increasing microtubule landing rate and enabling kinesin motility along microtubules.

A) An overlay of the Alphafold3 model of $MAP7^{CT}$ (residues 686-728) (purple envelope and ribbon) binding to $CC1^{KHC}$ onto the $CC1^{KLC}$ -$CC2^{KLC}$-CC4 kinesin autoinhibited structure (faded surface colors) revealing MAP7 binding induces steric hindrance with the $CC2^{KLC}$ and CC4 interface on $CC1^{KHC}$. Details in (**Figure S9; Figure S15**).
B) Kymographs of Kinesin reconstitution with MTs visualized by TIRF microscopy. Left panel, autoinhibited kinesin binds along MTs (left) and leads to transient and static association events. Right panel, in the presence of $MAP7D3^{CT}$, kinesin shows enhanced landing rates and activation of processive motility toward MT plus ends (left end).
C) Left panel, Quantitation of MT landing events for kinesin in the absence and presence of $MAP7D3^{CT}$. Right panel, Quantitation of processive motility events.
D) Model illustrating the microtubule-mediated transition and MAP7D3-driven activation of kinesin through disruption of the autoinhibited lambda conformation. Domains are color-coded as in **Figure 2**. Panels I–IV (bottom) depict the overall kinesin conformation and its transitions on the microtubule lattice in response to MAP7D3 binding. Top panels provide close-up views of specific domains and regions undergoing structural changes during activation. Activation begins when MT-bound MAP7 **(I)** binds to the KHC CC1 region, causing a steric clash that destabilizes and unfurls the autoinhibited complex **(II)**. This large-scale rearrangement sequentially **(1)** releases the motor domains for motility by unraveling the CC0 neck coiled-coil **(III-IV, central panels)** and **(2)** unmasks the KLC TPR cargo-binding sites by displacing the C-terminal inhibitory helices **(III-IV, top panels)**, rendering the motor fully active for transport **(IV)**.

Table I: Cryo-EM data collection, structure determination and model building statistics

Parameters	Motor-B-CC0-TPR-B	Motor-A-Tails	TPR-A-Central section	Coiled-coil Elbow region
Magnification	x			
Voltage (kV)	300			
Electron exposure (e/Å^{-2})	48			
Defocus range (µm)	-0.8 to -2.5			
Pixel size (Å)	0.926			
Symmetry imposed	C1			
No. of final particle images	103108		595495	30746
Map resolution FSC threshold (Å)	7.6	6.5	5.6	8.6
Initial model used	AlphaFold3 predictions			
Model resolution FSC threshold (Å)	0.5			
Model resolution (Å)	8			
Model composition				
Chains	4			
Non-hydrogen atoms	27751			
Protein	3476			
Nucleic acid	0			
Ligand	0			
R.M.S. deviations				
Bonds (Å)	0.003			
Angles (°)	0.542			
MolProbity score	1.99			
Clashscore	11.21			
Poor rotamers (%)	0.07			
Ramachandran plot				
Favored (%)	93.57			
Allowed (%)	6.26			
Disallowed (%)	0.17			

References:

1 Vale, R. D., Reese, T. S. & Sheetz, M. P. Identification of a novel force-generating protein, kinesin, involved in microtubule-based motility. *Cell* **42**, 39-50 (1985). https://doi.org:10.1016/s0092-8674(85)80099-4

2 Hirokawa, N., Noda, Y., Tanaka, Y. & Niwa, S. Kinesin superfamily motor proteins and intracellular transport. *Nature Reviews Molecular Cell Biology* **10**, 682-696 (2009). https://doi.org:10.1038/nrm2774

3 Vale, R. D. The Molecular Motor Toolbox for Intracellular Transport. *Cell* **112**, 467-480 (2003). https://doi.org:10.1016/S0092-8674(03)00111-9

4 Guedes-Dias, P. & Holzbaur, E. L. F. Axonal transport: Driving synaptic function. *Science* **366**, eaaw9997 (2019). https://doi.org:doi:10.1126/science.aaw9997

5 Verhey, K. J. & Hammond, J. W. Traffic control: regulation of kinesin motors. *Nature Reviews Molecular Cell Biology* **10**, 765-777 (2009). https://doi.org:10.1038/nrm2782

6 Lu, W. & Gelfand, V. I. Moonlighting Motors: Kinesin, Dynein, and Cell Polarity. *Trends in Cell Biology* **27**, 505-514 (2017). https://doi.org:10.1016/j.tcb.2017.02.005

7 Yildiz, A., Tomishige, M., Vale, R. D. & Selvin, P. R. Kinesin walks hand-over-hand. *Science* **303**, 676-678 (2004). https://doi.org:10.1126/science.1093753

8 Wirth, J. O. *et al.* MINFLUX dissects the unimpeded walking of kinesin-1. *Science* **379**, 1004-1010 (2023). https://doi.org:doi:10.1126/science.ade2650

9 Hackney, D. D., Levitt, J. D. & Suhan, J. Kinesin undergoes a 9 S to 6 S conformational transition. *Journal of Biological Chemistry* **267**, 8696-8701 (1992). https://doi.org:https://doi.org/10.1016/S0021-9258(18)42499-4

10 Cai , D., Hoppe , A. D., Swanson , J. A. & Verhey , K. J. Kinesin-1 structural organization and conformational changes revealed by FRET stoichiometry in live cells. *Journal of Cell Biology* **176**, 51-63 (2007). https://doi.org:10.1083/jcb.200605097

11 Hirokawa, N. *et al.* Submolecular domains of bovine brain kinesin identified by electron microscopy and monoclonal antibody decoration. *Cell* **56**, 867-878 (1989).

12 Tan, Z. *et al.* Autoinhibited kinesin-1 adopts a hierarchical folding pattern. *eLife* **12**, RP86776 (2023). https://doi.org:10.7554/eLife.86776

13 Weijman, J. F. *et al.* Molecular architecture of the autoinhibited kinesin-1 lambda particle. *Science Advances* **8**, eabp9660 (2022). https://doi.org:doi:10.1126/sciadv.abp9660

14 Carrington, G. *et al.* A multiscale approach reveals the molecular architecture of the autoinhibited kinesin KIF5A. *J Biol Chem* **300**, 105713 (2024). https://doi.org:10.1016/j.jbc.2024.105713

15 Cross, J. A. & Dodding, M. P. Motor–cargo adaptors at the organelle–cytoskeleton interface. *Current Opinion in Cell Biology* **59**, 16-23 (2019). https://doi.org:https://doi.org/10.1016/j.ceb.2019.02.010

16 Pernigo, S., Lamprecht, A., Steiner, R. A. & Dodding, M. P. Structural basis for kinesin-1: cargo recognition. *Science* **340**, 356-359 (2013).

17 Heber, S. *et al.* Tropomyosin 1-I/C coordinates kinesin-1 and dynein motors during oskar mRNA transport. *Nat Struct Mol Biol* **31**, 476-488 (2024). https://doi.org:10.1038/s41594-024-01212-x

18 Fu, M.-m. & Holzbaur, E. L. JIP1 regulates the directionality of APP axonal transport by coordinating kinesin and dynein motors. *Journal of Cell Biology* **202**, 495-508 (2013).
19 Sun, F., Zhu, C., Dixit, R. & Cavalli, V. Sunday Driver/JIP3 binds kinesin heavy chain directly and enhances its motility. *The EMBO journal* **30**, 3416-3429 (2011).
20 Cross, J. A., Woolfson, D. N. & Dodding, M. P. Kinesin-1 captures RNA cargo in its adaptable coils. *Genes Dev* **35**, 937-939 (2021). https://doi.org:10.1101/gad.348691.121
21 Yildiz, A. Mechanism and regulation of kinesin motors. *Nat Rev Mol Cell Biol* **26**, 86-103 (2025). https://doi.org:10.1038/s41580-024-00780-6
22 Chiba, K., Ori-McKenney, K. M., Niwa, S. & McKenney, R. J. Synergistic autoinhibition and activation mechanisms control kinesin-1 motor activity. *Cell Rep* **39**, 110900 (2022). https://doi.org:10.1016/j.celrep.2022.110900
23 Hooikaas, P. J. *et al.* MAP7 family proteins regulate kinesin-1 recruitment and activation. *J Cell Biol* **218**, 1298-1318 (2019). https://doi.org:10.1083/jcb.201808065
24 Ferro, L. S. *et al.* Structural and functional insight into regulation of kinesin-1 by microtubule-associated protein MAP7. *Science* **375**, 326-331 (2022). https://doi.org:doi:10.1126/science.abf6154
25 Sahabandu, N. *et al.* Active microtubule-actin cross-talk mediated by a nesprin-2G–kinesin complex. *Science Advances* **11**, eadq4726 (2025). https://doi.org:doi:10.1126/sciadv.adq4726
26 Stark, H. GraFix: stabilization of fragile macromolecular complexes for single particle cryo-EM. *Methods Enzymol* **481**, 109-126 (2010). https://doi.org:10.1016/s0076-6879(10)81005-5
27 Kaan, H. Y., Hackney, D. D. & Kozielski, F. The structure of the kinesin-1 motor-tail complex reveals the mechanism of autoinhibition. *Science* **333**, 883-885 (2011). https://doi.org:10.1126/science.1204824
28 Atherton, J. *et al.* Microtubule association induces a Mg-free apo-like ADP pre-release conformation in kinesin-1 that is unaffected by its autoinhibitory tail. *bioRxiv*, 2024.2011.2011.622991 (2024). https://doi.org:10.1101/2024.11.11.622991
29 Friedman, D. S. & Vale, R. D. Single-molecule analysis of kinesin motility reveals regulation by the cargo-binding tail domain. *Nature cell biology* **1**, 293-297 (1999).
30 Coy, D. L., Hancock, W. O., Wagenbach, M. & Howard, J. Kinesin's tail domain is an inhibitory regulator of the motor domain. *Nature Cell Biology* **1**, 288-292 (1999). https://doi.org:10.1038/13001
31 Stock, M. F. *et al.* Formation of the compact confomer of kinesin requires a COOH-terminal heavy chain domain and inhibits microtubule-stimulated ATPase activity. *Journal of Biological Chemistry* **274**, 14617-14623 (1999).
32 Yip, Y. Y. *et al.* The light chains of kinesin-1 are autoinhibited. *Proc Natl Acad Sci U S A* **113**, 2418-2423 (2016). https://doi.org:10.1073/pnas.1520817113
33 Pernigo, S. *et al.* Structural basis for isoform-specific kinesin-1 recognition of Y-acidic cargo adaptors. *eLife* **7**, e38362 (2018). https://doi.org:10.7554/eLife.38362
34 Kozielski, F. *et al.* The crystal structure of dimeric kinesin and implications for microtubule-dependent motility. *Cell* **91**, 985-994 (1997). https://doi.org:10.1016/s0092-8674(00)80489-4

35 Benoit, M., Rao, L., Asenjo, A. B., Gennerich, A. & Sosa, H. Cryo-EM unveils kinesin KIF1A's processivity mechanism and the impact of its pathogenic variant P305L. *Nat Commun* **15**, 5530 (2024). https://doi.org:10.1038/s41467-024-48720-4
36 Monroy, B. Y. *et al.* Competition between microtubule-associated proteins directs motor transport. *Nat Commun* **9**, 1487 (2018). https://doi.org:10.1038/s41467-018-03909-2
37 Verhey, K. J., Kaul, N. & Soppina, V. Kinesin Assembly and Movement in Cells. *Annual Review of Biophysics* **40**, 267-288 (2011). https://doi.org:https://doi.org/10.1146/annurev-biophys-042910-155310
38 Abramson, J. *et al.* Accurate structure prediction of biomolecular interactions with AlphaFold 3. *Nature* **630**, 493-500 (2024). https://doi.org:10.1038/s41586-024-07487-w
39 Vale, R. D. & Milligan, R. A. The way things move: looking under the hood of molecular motor proteins. *Science* **288**, 88-95 (2000). https://doi.org:10.1126/science.288.5463.88
40 Hackney, D. D. & Stock, M. F. Kinesin's IAK tail domain inhibits initial microtubule-stimulated ADP release. *Nat Cell Biol* **2**, 257-260 (2000). https://doi.org:10.1038/35010525
41 Suloway, C. *et al.* Automated molecular microscopy: the new Leginon system. *J Struct Biol* **151**, 41-60 (2005). https://doi.org:10.1016/j.jsb.2005.03.010
42 Bouvette, J. *et al.* Beam image-shift accelerated data acquisition for near-atomic resolution single-particle cryo-electron tomography. *Nature Communications* **12**, 1957 (2021). https://doi.org:10.1038/s41467-021-22251-8
43 Guo, H. *et al.* Electron-event representation data enable efficient cryoEM file storage with full preservation of spatial and temporal resolution. *IUCrJ* **7**, 860-869 (2020). https://doi.org:10.1107/s205225252000929x
44 Scheres, S. H. W. RELION: Implementation of a Bayesian approach to cryo-EM structure determination. *Journal of Structural Biology* **180**, 519-530 (2012). https://doi.org:https://doi.org/10.1016/j.jsb.2012.09.006
45 Rohou, A. & Grigorieff, N. CTFFIND4: Fast and accurate defocus estimation from electron micrographs. *J Struct Biol* **192**, 216-221 (2015). https://doi.org:10.1016/j.jsb.2015.08.008
46 Punjani, A., Rubinstein, J. L., Fleet, D. J. & Brubaker, M. A. cryoSPARC: algorithms for rapid unsupervised cryo-EM structure determination. *Nature Methods* **14**, 290-296 (2017). https://doi.org:10.1038/nmeth.4169
47 Bepler, T. *et al.* Positive-unlabeled convolutional neural networks for particle picking in cryo-electron micrographs. *Nature Methods* **16**, 1153-1160 (2019). https://doi.org:10.1038/s41592-019-0575-8
48 Lee, B. G. *et al.* Cryo-EM structures of holo condensin reveal a subunit flip-flop mechanism. *Nat Struct Mol Biol* **27**, 743-751 (2020). https://doi.org:10.1038/s41594-020-0457-x
49 Punjani, A. & Fleet, D. J. 3DFlex: determining structure and motion of flexible proteins from cryo-EM. *Nature Methods* **20**, 860-870 (2023). https://doi.org:10.1038/s41592-023-01853-8
50 Morin, A. *et al.* Collaboration gets the most out of software. *eLife* **2**, e01456 (2013). https://doi.org:10.7554/eLife.01456

51 Liebschner, D. *et al.* Macromolecular structure determination using X-rays, neutrons and electrons: recent developments in Phenix. *Acta Crystallogr D Struct Biol* **75**, 861-877 (2019). https://doi.org:10.1107/s2059798319011471
52 Pettersen, E. F. *et al.* UCSF ChimeraX: Structure visualization for researchers, educators, and developers. *Protein Sci* **30**, 70-82 (2021). https://doi.org:10.1002/pro.3943
53 Williams, C. J. *et al.* MolProbity: More and better reference data for improved all-atom structure validation. *Protein Sci* **27**, 293-315 (2018). https://doi.org:10.1002/pro.3330
54 Lagerwaard, I. M., Albanese, P., Jankevics, A. & Scheltema, R. A. Xlink Mapping and AnalySis (XMAS) - Smooth Integrative Modeling in ChimeraX. *bioRxiv*, 2022.2004.2021.489026 (2022). https://doi.org:10.1101/2022.04.21.489026
55 Edelstein, A. D. *et al.* Advanced methods of microscope control using muManager software. *J Biol Methods* **1** (2014). https://doi.org:10.14440/jbm.2014.36

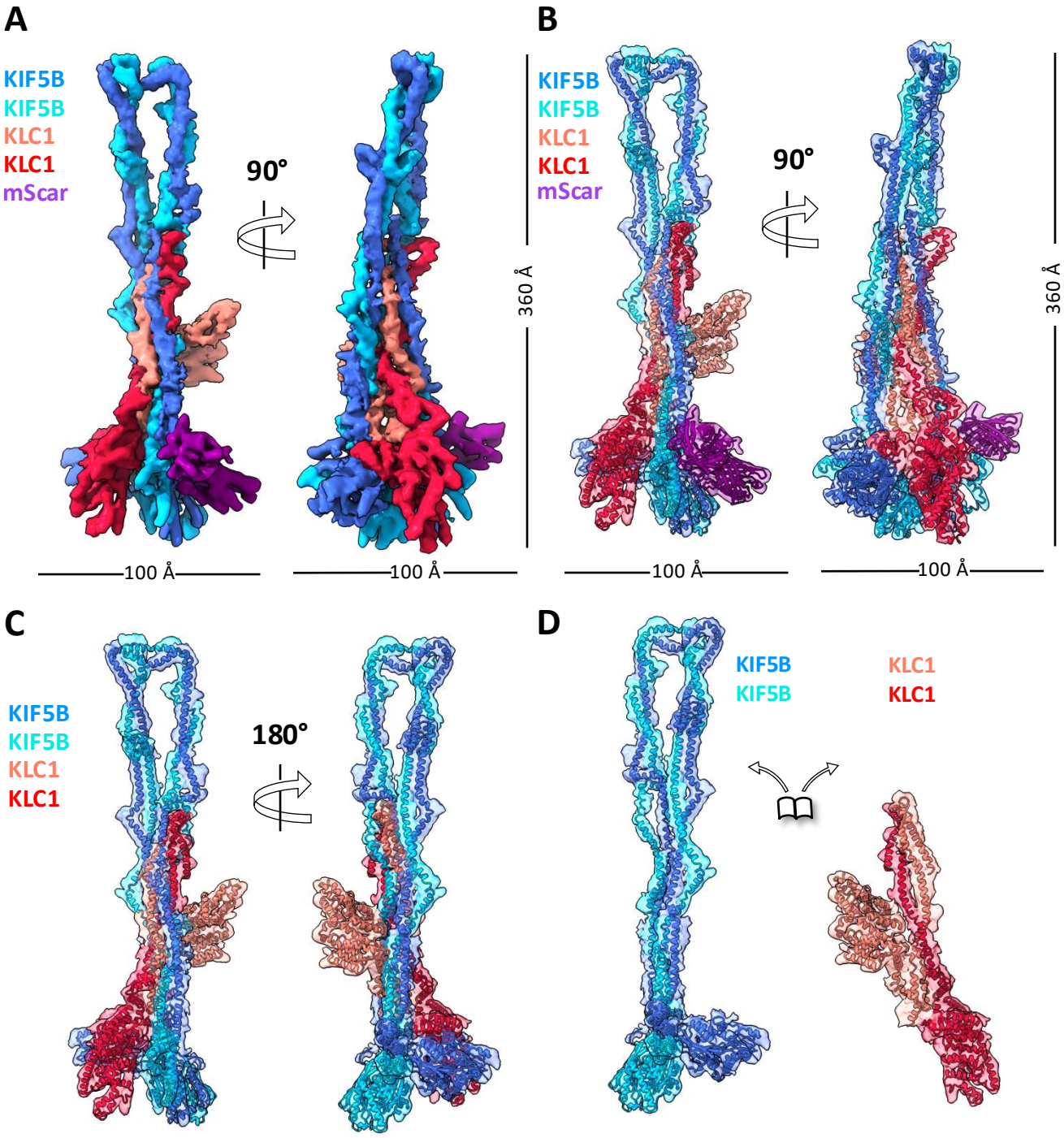
A
KIF5B
KIF5B
KLC1
KLC1
mScar
90°
360 Å
100 Å
100 Å
B
KIF5B
KIF5B
KLC1
KLC1
mScar
90°
360 Å
100 Å
100 Å
C
KIF5B
KIF5B
KLC1
KLC1
180°
D
KIF5B
KIF5B
KLC1
KLC1

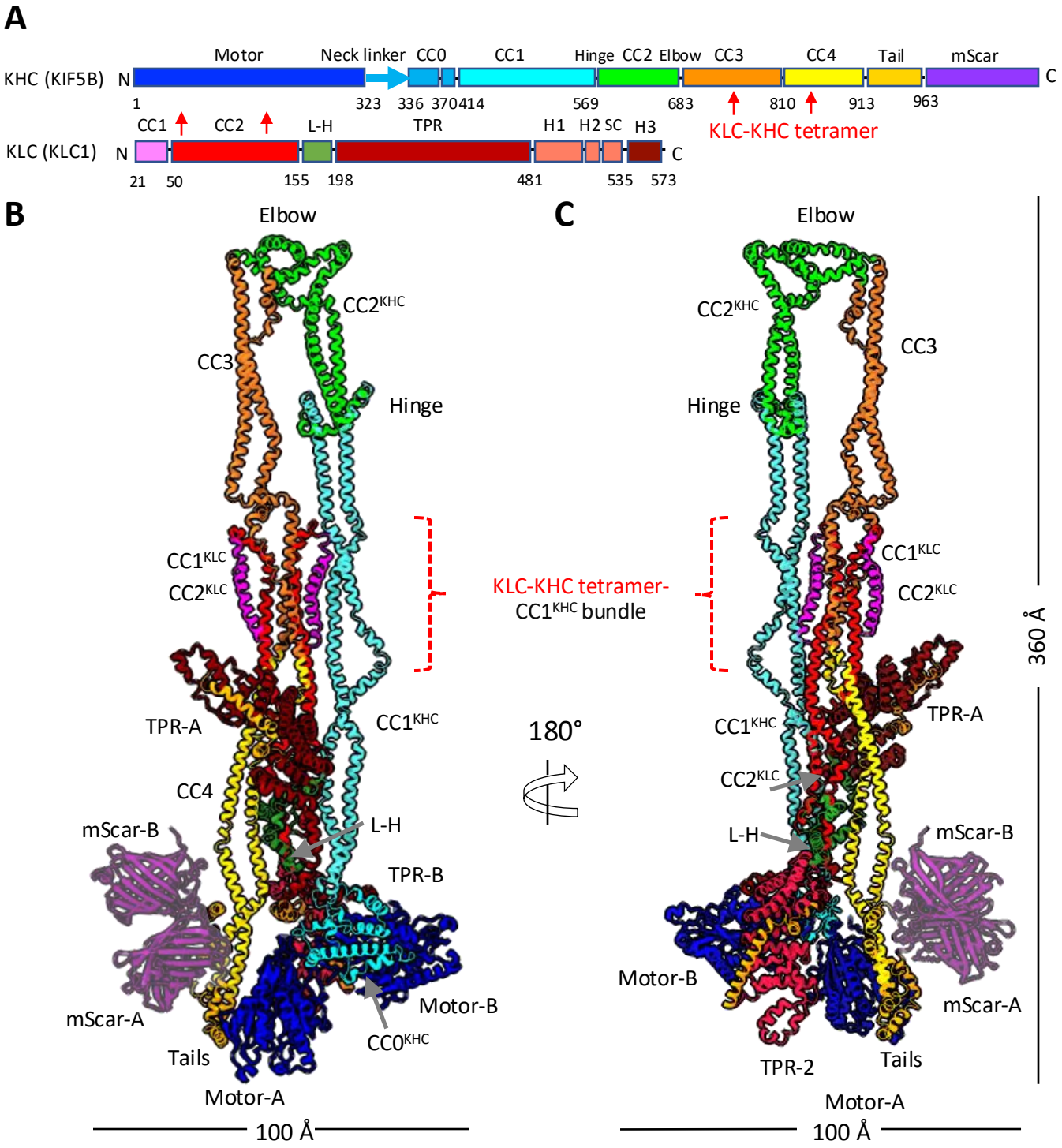
A
KHC (KIF5B)
N
C
Motor
Neck linker
CC0
CC1
Hinge
CC2
Elbow
CC3
CC4
Tail
mScar
1
323
336
370
414
569
683
810
913
963
KLC-KHC tetramer
KLC (KLC1)
CC1
CC2
L-H
TPR
H1
H2
SC
H3
21
50
155
198
481
535
573
B
Elbow
CC2KHC
CC3
Hinge
CC1KLC
CC2KLC
TPR-A
CC1KHC
CC4
L-H
mScar-B
TPR-B
mScar-A
Motor-B
CC0KHC
Tails
Motor-A
100 Å
KLC-KHC tetramer-
CC1KHC bundle
180°
C
Elbow
CC2KHC
CC3
Hinge
CC1KLC
CC2KLC
TPR-A
CC1KHC
CC2KLC
L-H
mScar-B
Motor-B
mScar-A
TPR-2
Tails
Motor-A
100 Å
360 Å

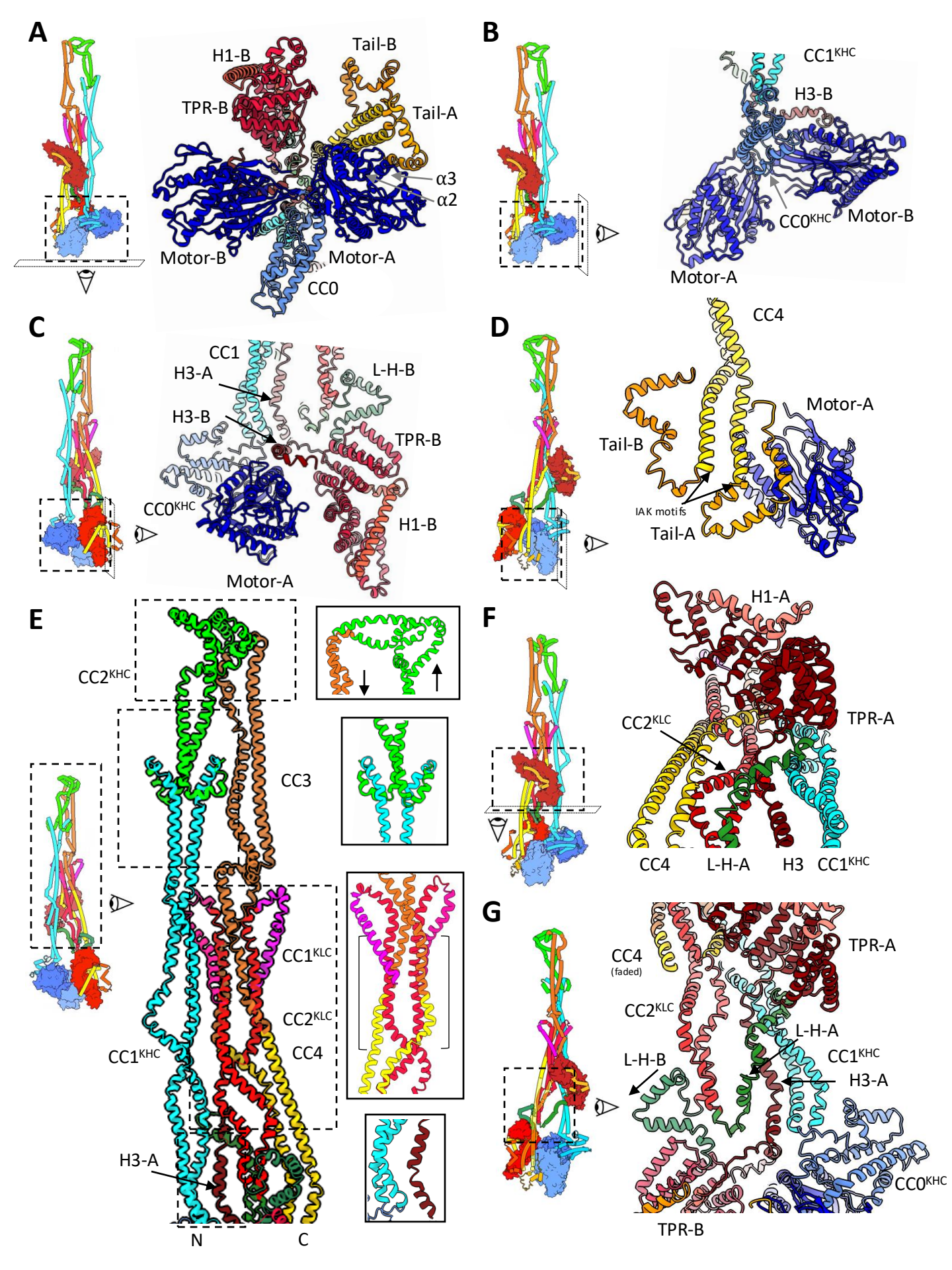
A
H1-B
Tail-B
TPR-B
Tail-A
α3
α2
Motor-B
Motor-A
CC0
B
CC1KHC
H3-B
CC0KHC
Motor-B
Motor-A
C
CC1
H3-A
L-H-B
H3-B
TPR-B
CC0KHC
H1-B
Motor-A
D
CC4
Motor-A
Tail-B
IAK motifs
Tail-A
E
CC2KHC
CC3
CC1KLC
CC2KLC
CC4
CC1KHC
H3-A
N
C
F
H1-A
CC2KLC
TPR-A
CC4
L-H-A
H3
CC1KHC
G
CC4
(faded)
TPR-A
CC2KLC
L-H-A
L-H-B
CC1KHC
H3-A
CC0KHC
TPR-B

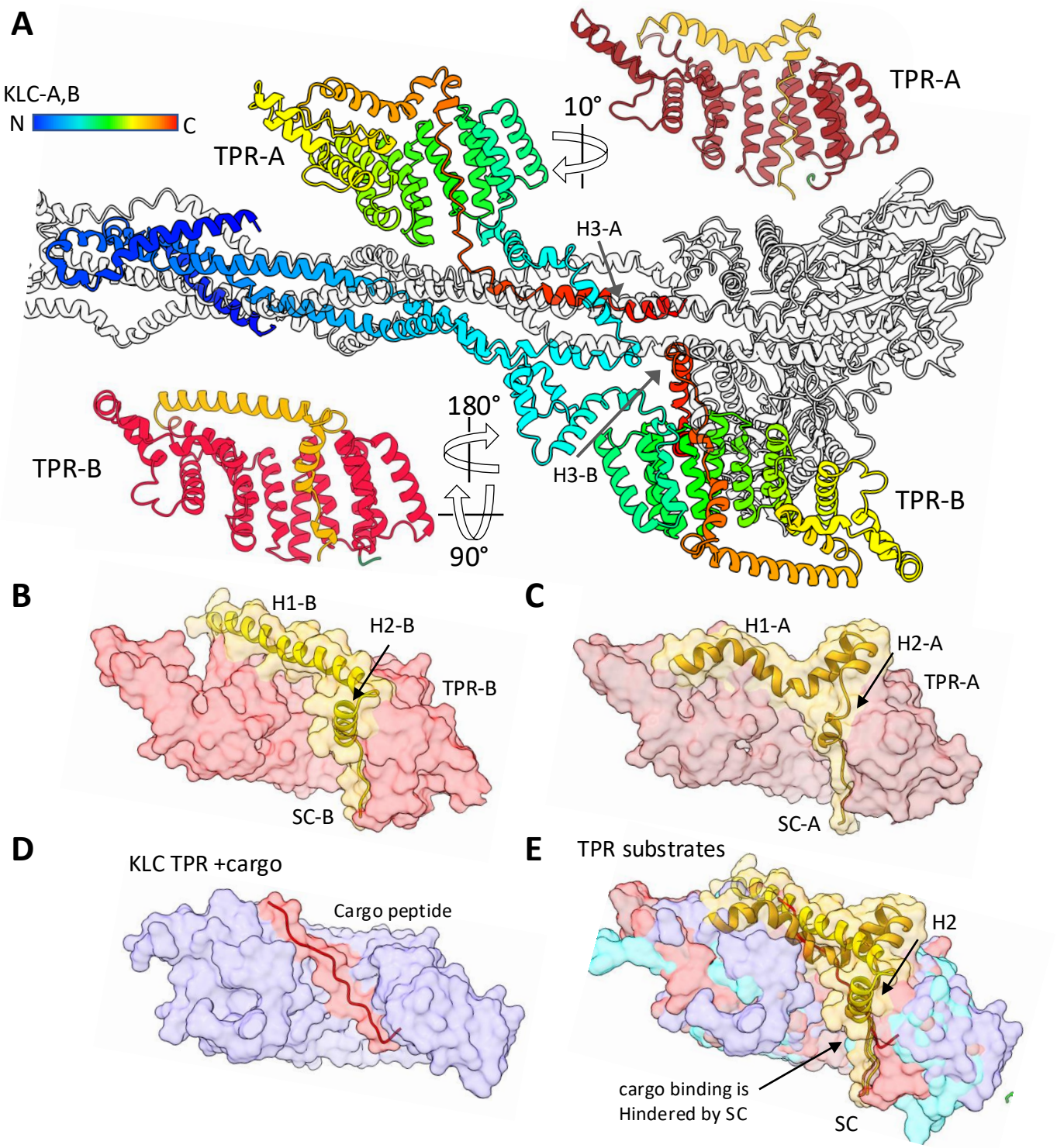
A
KLC-A,B
N
C
TPR-A
10°
TPR-A
H3-A
180°
TPR-B
H3-B
TPR-B
90°
B
H1-B
H2-B
TPR-B
SC-B
C
H1-A
H2-A
TPR-A
SC-A
D
KLC TPR +cargo
Cargo peptide
E
TPR substrates
H2
cargo binding is
Hindered by SC
SC

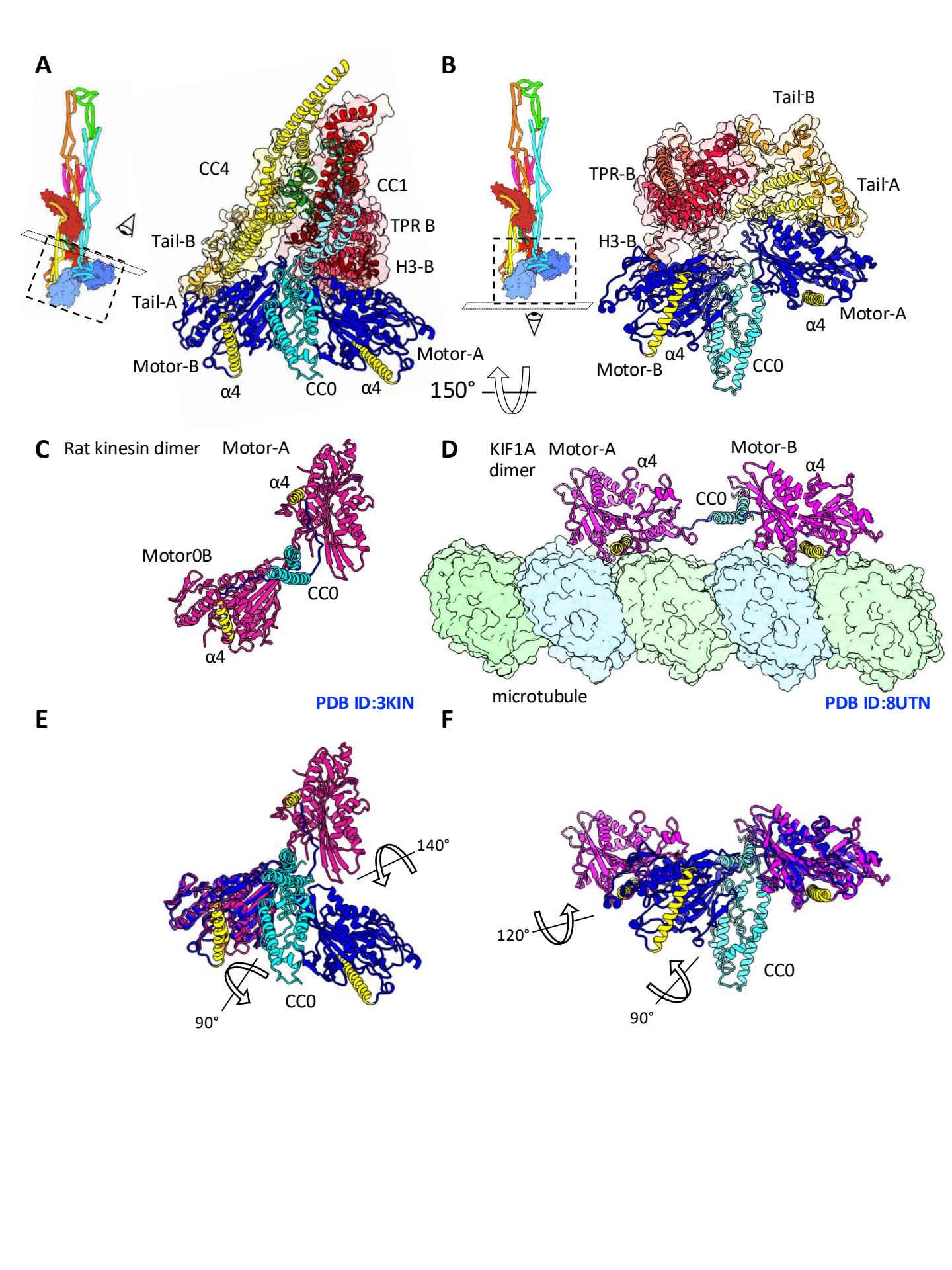
A
CC4
CC1
TPR B
Tail-B
H3-B
Tail-A
Motor-B
α4
CC0
α4
Motor-A
150°
B
Tail-B
TPR-B
Tail-A
H3-B
Motor-A
α4
α4
Motor-B
CC0
C
Rat kinesin dimer
Motor-A
α4
Motor0B
CC0
α4
PDB ID:3KIN
D
KIF1A dimer
Motor-A
α4
Motor-B
α4
CC0
microtubule
PDB ID:8UTN
E
140°
90°
CC0
F
120°
90°
CC0

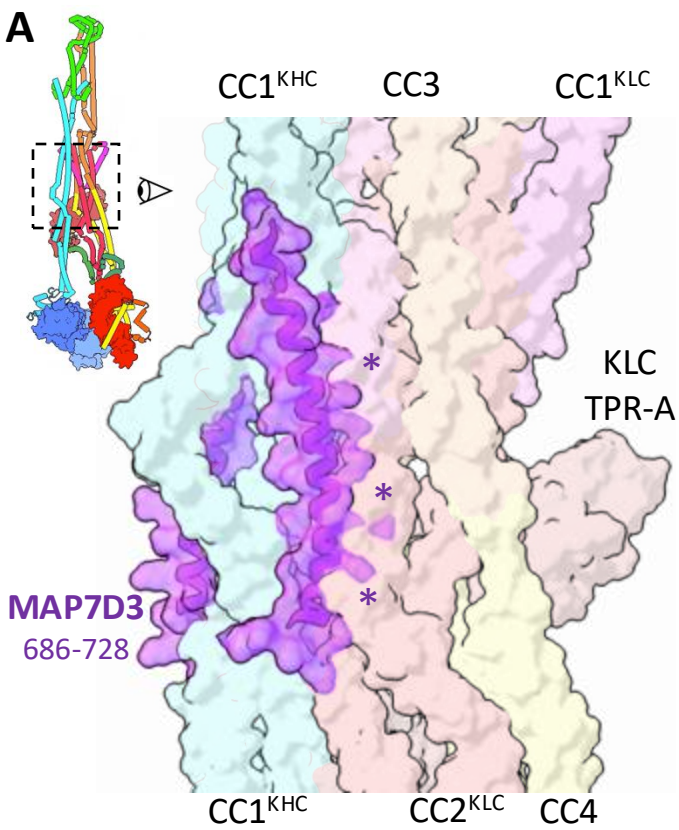
A
CC1KHC
CC3
CC1KLC
KLC
TPR-A
MAP7D3
686-728
CC1KHC
CC2KLC
CC4

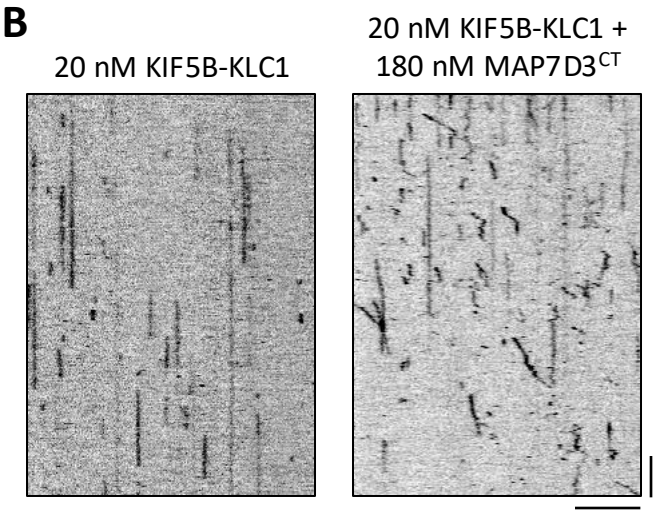
B
20 nM KIF5B-KLC1
20 nM KIF5B-KLC1 +
180 nM MAP7D3CT

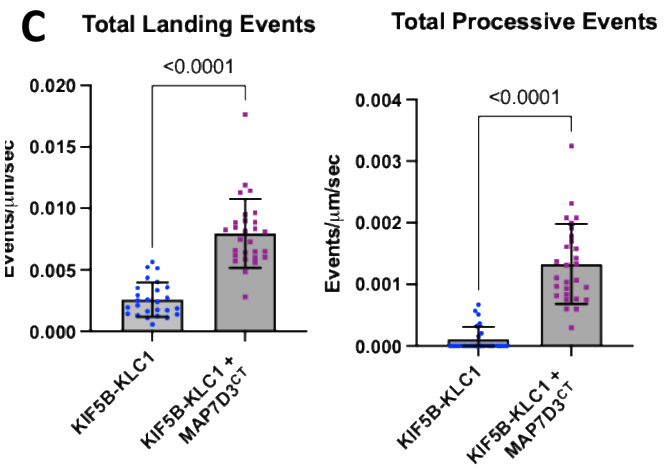
C
Total Landing Events
Total Processive Events
<0.0001
<0.0001
Events/µm/sec
0.020
0.015
0.010
0.005
0.000
0.004
0.003
0.002
0.001
0.000
KIF5B-KLC1
KIF5B-KLC1 + MAP7D3CT

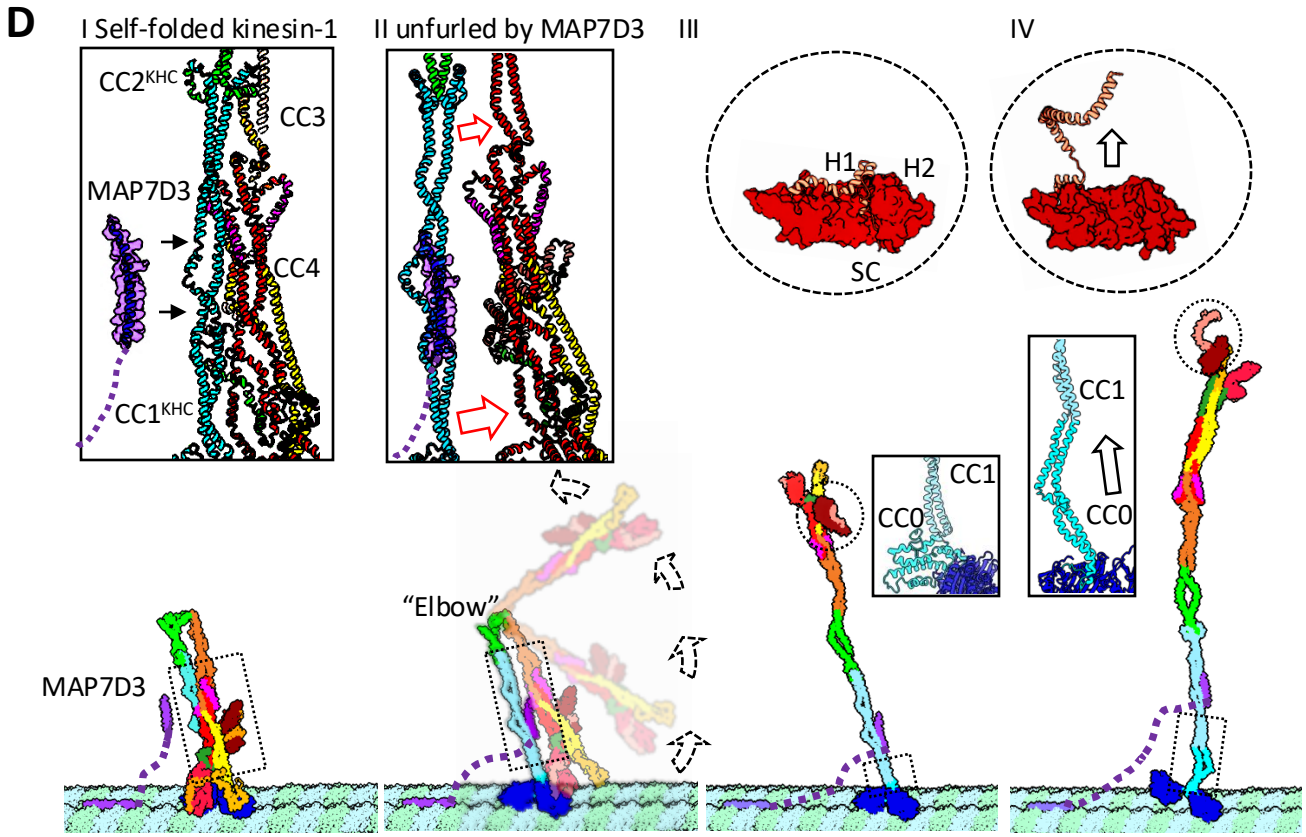
D
I Self-folded kinesin-1
II unfurled by MAP7D3
III
IV
CC2KHC
CC3
MAP7D3
CC4
CC1KHC
H1
H2
SC
CC1
CC0
CC1
CC0
"Elbow"
MAP7D3

Supplementary Text

Validating the Autoinhibited Structure Using Crosslinking Mass Spectrometry Data

To validate our cryo-EM-derived structure, we tested whether models based on it could better explain previously published crosslinking mass spectrometry (XLMS) data[12] compared to earlier models derived from negative-stain EM[12-14]. We generated three computational models from our KIF5B-KLC1 structure: 1) the full KIF5B-KLC1 heterotetramer, 2) a KIF5B homodimer created by removing the KLC1 subunits, and 3) a KIF5C-KLC1 heterotetramer created by modeling KIF5C-specific residues onto the KIF5B backbone. We then analyzed how well these models satisfied existing intra-molecular XLMS datasets for each species, focusing on whether the models could validate the proposed folding architecture.

Our analysis revealed that the cryo-EM-based models explain significantly more crosslinks than previously possible, confirming their accuracy. For the KIF5B-KLC1 heterotetramer, our model satisfies 123 crosslinks at a 24-Å distance cutoff and 169 at 50-Å (**Figure S12**). The satisfied crosslinks include key interactions between the KLC coiled-coils and KHC coiled-coil 4 (CC4), and between the KLC TPR domains and CC4 (**Table S1**). Few crosslinks to the motor domains were satisfied, which we attribute to the high flexibility of the motors observed during data processing (**Figure S5**). Overall, our KIF5B-KLC1 model shows superior alignment with the XLMS data, correctly positioning domains like the C-terminal tail and CC0 that were unresolved in the negative-stain model[24] [12].

For the KIF5B homodimer, our model satisfied 119 crosslinks at 24-Å and 167 at 50-Å (**Figure S14**), a substantial increase from the 22 crosslinks explained by the NSEM-based model [12]. The model accounts for extensive intra-dimer crosslinks between the motor domains, across multiple coiled-coil regions, between the motor and CC4, and a key link between the IAK tail motif and CC4 (**Table S1**). The similarity in crosslinking patterns suggests that the KIF5B homodimer adopts a fold nearly identical to its conformation within the heterotetramer, supporting the view that KLCs primarily stabilize a pre-existing autoinhibited state.

Finally, our KIF5C-KLC1 model satisfied 214 crosslinks at 24-Å and 374 at 50-Å (**Figure S13**). The higher number of satisfied interactions is consistent with previous findings that the KIF5C-KLC1 complex is more stable than its KIF5B counterpart[12]. This model explained additional crosslinks not observed for KIF5B-KLC1, including contacts between the motor and TPR domains and between a TPR domain and the KHC tail (**Table S1**). Together, these analyses demonstrate that the overall autoinhibited architecture is conserved among kinesin-1 isotypes. Our structure provides a high-resolution framework that explains numerous previously unmappable crosslinks[12-14]., thereby validating our model and offering a more detailed understanding of the interactions governing kinesin-1 regulation.

Supplementary Figure Legends

Figure S1: Preparation scheme of Kinesin KIF5B-KLC1 sample for Cryo-EM.

Top Left, purified KIF5B-KLC1 solution crosslinking experiment with glutaraldehyde. Lane:1 Marker, Lane 3: control KIF5B-mscarlet-KLC1, lane 5: 0.02% glutaraldehyde, lane 7: 0.04% glutaraldehyde, lane 9: 0.08% glutaraldehyde, lane 11: 0.16% glutaraldehyde. Samples were crosslinked at room temperature for 30 minutes and quenched and loaded on the gel to find optimal crosslinker concentration. Top right, using the best crosslinker concentration multiple tubes "GraFix" experiments were set up to mildly crosslink the sample, which were pooled based on mass photometry-based screening shown on the bottom right panel. Crosslinked sample was iteratively vitrified along with screening for Cryo-EM data acquisition shown on bottom left panel.

Figure S2: Scheme for Cryo-EM data processing strategy.
Cryo-EM movies were collected in EER format which then processed in RELION followed by autopicking and extraction in 200-pixel box (4x binned). 2D classification used for good set of particles and topaz trained to pick more and 2D classify which then aligned to negative stain map. Aligned particles were passthrough iterative heterogeneous refine followed by 3D refine and 2D and 3D classification to select final particle set which were then polished and passed through the same cycle as above classification approach. Good particles were then flexible refined and local refined for final map generation. Each set of steps of in the single particle structural analysis is labeled with an associated supplementary **Figure S2-S7**.

Figure S3: Cryo-EM processing for single particle alignment.
Four datasets pre-processed and picked separately which then pass thorough the approach presented in the figure where particles in big box (800 pixel, unbinned) were classified extensively to select only good particles. 2D classification shows mostly closed Kinesin-1 particles with top and side views and some open Kinesin-1 particles. These particles were 4x binned and aligned with T=0 classification with 1 class and 3D refined which then used for further processing described in **Figure S4**.

Figure S4: Cryo-EM processing for selection of single particles for final refinements.
Each dataset was picked and aligned with the negative stain map and iterative classification approach where rounds of heterogeneous refinement followed by 3D-refinements and further classification selected good sets of particles which were flexible refined and classified again before final 3D refine and local refinement shown in **Figures S5 and S6**.

Figure S5: Cryo-EM processing of Kinesin lambda particles.
All particles from four datasets were merged and 3D-refined iteratively followed by 2D without alignment. Placement of model followed by and re-extraction in small box (150 pixel, 2x binned) was local refined for the core of Kinesin-1 consists of KLC (CCs, TPR-B) and KHC (part of CC1 and CC4). Merged data was refined and 3D classified without alignment to select 103108 particles with Motor density clearly present for both KHCs. Placement of models and re-extraction into

small box (150 pix, 2x binned) was used for final local refinements for different parts of Motors, TPR(KLC) and tails.

Figure S6: Cryo-EM data processing of the elbow region of Kinesin-1.
103k particles separated in **Figure S5** was 3D refined, recenter and reextracted followed by flexible refinement and assignments of densities were used to generate and model-based map to local refine the whole structure and 3D variability analysis (shown in **Figure S8**) was to separate 30k-particles which shows clear turn-around of elbow was 3D-refined by homogeneous reconstruction followed by local refinements.

Figure S7: Final maps, FSCs and generation of full Kinesin autoinhibited structure map.
Local refined maps for each subregion are shown on left followed by their FSCs and local resolution Res maps for each subregion. on the right which were then aligned and Vop-merged in chimera for generating full-length Kinesin density map for model building.

Figure S8: Map and Model close-up showing building of Kinesin-1 domain placements.

(A) Motors map and model placements of KHCs are shown in blue where individual motors are shown on left and dimer on right.
(B) End of KHC CC4 and tails map to model showing without mscarlets on left, with mscarlet on middle and just mscarlet on right.
(C) Map to model of CC0 and neck linker.
(D) Map to model of TPRs.
(E) Map to model of central bundle composed of CC1 and CC4 of KHC and CCs of KLCs
(F) Map to model of the elbow structure of $CC2^{KHC}$, CC3.

Figure S9: Surface representation showing buried surfaces between KHC and KLC in KIF5B/KLC1 cryo-EM structure.
Two views at 180° of KIF5B/KLC1 structure showing the buried surface where at the left full complex is shown and the right KHC and KLC are shown as separate map-to-model in similar color coding. Buried surface area of 5550 $Å^2$ is shown in red.

Figure S10: Comparison of Kinesin autoinhibited structures from Cryo-EM, AlphaFold and negative structures.

(A) Left panel, Multiple rotated views of AlphaFold3[38] prediction of KIF5B-mScarlet/KLC1 shown in rainbow colors for both KHC and KLC subunits. Right panel, Alphafold3 pLDDT 2D-plot showing the accuracy of domain prediction.
(B) Top panel, Linear domain representation of KIF5B-KLC1. Bottom panel, Side by side Comparison of Kinesin structural models in consistent color coding as shown in linear domain mapping shown in top pane. Left panels Cryo-EM model based on this study , middle panels the Kinesin-1 Alphafold3 (as shown in A), left panel the negative stain EM model described by Tan et al[12]. There are no mScarlets shown in negative stain model.

Figure S11: Conservation plot of Kinesin, accompanying close-up views in Figure 2.

A) Full Conservation plot of Kinesin heterotetramer showing the full autoinhibited structure.

B) Close-up plot showing Motor-tail-TPR interfaces. The motor domains are very conserved with some moderate conservation in CC0 but highly variable C-terminal tails. The KLC TPR domains are highly conserved.
C) Close up view of Conservation plot showing interfaces of TPR-B/motor-B/H3 where the KLC L-H and H1 are less conserved but H3 is moderately conserved.
D) Conservation plot of KHC and KLC coiled-coils showing the interfaces for self-folding are relatively well conserved. The interface of H3/CC1$^{KHC+KLC}$/CC4 coiled-coils (8 bundles) is very conserved. Interface of CC1-KLC(CCs)-CC4 is well conserved on the interacting sites. elbow structure is very conserved.
E) Conservation plot of KLC-TPR-A on CC4-CC1 is in interface with high conservation while the H3 is variable.
F) Conservation plot showing KHC motor-A and C-terminal tails showing tails are variable, but their regions that bind the motors are well-conserved site while their C-termini are less conserved.
G) Conservation plot of the central core showing the KHC coiled-coils and KLC-TPR are well conserved. H3 is partially conserved.

Figure S12: Plotting the Human KIF5B-KLC1 XLMS[12] onto the kinesin autoinhibited structure.
A) shows an overall view of the autoinhibited KIF5B-KLC1 heterotetramer model with the crosslinks.
B) close-up and bottom of the KHC motor A, B-tail-KLC-TPR-B interfaces.
C) side-view of panel B.
D) Side view of the back-folded CC2^{KLC} and CC4 onto CC1^{KHC} bound by the KLC-TPR-A.

Figure S13: Plotting the Human KIF5C-KLC1 XLMS[12] onto a homology model of the KIF5C-KLC1 in the autoinhibited state based on the cryo-EM structure.
A) shows an overall view of XLMS crosslinks on the homology KIF5C-KLC1 autoinhibited model
B) close-up and bottom of the KHC motor A, B-tail-KLC-TPR-B interfaces.
C) side-view of panel B.
D) Side view of the back-folded CC2^{KLC} and CC4 onto CC1^{KHC} bound by the KLC-TPR-A

Figure S15: identifying the MAP7D3 binding site on KHC KIF5B using Alphafold3.
A) Alphafold3 results of the MAP7D3^{CT} dimer with KHC KIF5B residues 1-587.
B) Trimmed model reveals that MAP7D3 residues 680-729 binds to KHC-CC1 405-587.
C) Comparison of trimmed model in B to overlaid MAP7D3 model onto Kinesin-1 autoinhibited structure reveals MAP7D3 sterically competes with KHC-CC3-CC4 /CC2^{KLC} binding onto CC1^{KHC}.
D) Close up of the boxed view in C.

Table S1: Structure based analysis of KIF5B-KLC1, KIF5C-KLC1, KIF5B dimer XLMS data from Tan et al[12]

Model	Domains crosslinked	Residues							
KIF5B dimer	Motor A-B	Lys159-Lys222							
	CC0	Lys350-Lys350							
	CC1-CC3	Lys540-Lys766							
	CC2- "hinge"	Lys596-Lys609							
	elbow	Lys657-Lys657	Lys685-Lys690	Lys679-Lys690					
	CC3	Lys754-Lys754							
	CC4	Lys803-Lys803	Lys815-Lys815	Lys831-Lys831	Lys909-Lys909				
	IAK tails to CC4	Lys922-Lys903	Lys922-Lys909						
	Motor(A)-CC4	Lys67-Lys903	Lys71-Lys903	Lys67-Lys909	Lys71-Lys909				
KIF5B-KLC1	Motor A-B	Lys159-Lys222							
	CC0	Lys394-Lys420	Lys402-Lys420						
	CC2- "hinge"	Lys560-Lys598	Lys575-Lys598	Lys575-Lys596					
	elbow	Lys679-Lys690							
	CC3	Lys753-Lys753	Lys755-Lys755						
	CC4	Lys803-Lys803	Lys815-Lys815	Lys909-Lys909					
	IAK tails to CC4	Lys922-Lys903	Lys922-Lys909						
	Motor(A)-CC4	Lys67-Lys909	Lys67-Lys909	Lys98-Lys903	Lys187-Lys909	Lys213-Lys909			
	KLC-CCs and KHC-CC4	Lys27-Lys803	Lys27-Lys793	Lys29-Lys815	Lys74-Lys803	Lys133-Lys864	Lys561-Lys849		
	KLC CC2-H3	Lys133-Lys561							
	KLC H3's	Lys561-Lys561							
	KLC-TPR(B) to CC4	Lys272-Lys882	Lys457-Lys903	Lys468-Lys909					
	KLC-SC to KHC-CC4	Lys518-Lys903							
	KLC-TPR(A) to CC4	Lys518-Lys815	Lys 518-Lys846						
KIF5C-KLC1	Motor A-B	Lys160-Lys222							
	CC0-CC4	Lys345-Lys887	Lys348-Lys887	Lys350-Lys884					
	"hinge"	Lys571-Lys571	Lys556-Lys599						
	"hinge"-CC4	Lys571-Lys730	Lys593-Lys741						
	CC2	Lys618-Lys618							
	elbow	Lys639-Lys639	Lys653-Lys653	Lys685-Lys685	Lys687-Lys687				
	CC3	Lys700-Lys700	Lys716-Lys716	Lys730-Lys730	Lys755-Lys755				
	CC4	Lys766-Lys766	Lys769-Lys769	Lys785-Lys785	Lys803-Lys803	Lys815-Lys815	Lys831-Lys831	Lys905-Lys905	Lys911-Lys911
	CC4-tail	Lys911-Lys924	Lys905-Lys957	Lys911-Lys957					
	CC4-motor	Lys34-Lys911	Lys68-Lys905	Lys72-Lys911	Lys99-Lys911	Lys188-Lys911			
	Motor-Tail	Lys68-Lys957	Lys72-Lys957	Lys99-Lys957	Lys167-Lys957				
	KLC-CCs to CC4	Lys27-Lys803	Lys29-Lys831	Lys27-Lys814	Lys27-Lys815	Lys39-Lys803	Lys57-Lys776	Lys58-Lys776	Lys103-Lys815
	KLC-CC to H3	Lys130-Lys561	Lys133-Lys561						
	KLC-H3 to KHC-CC4	Lys561-Lys846	Lys561-Lys849	Lys561-Lys884	Lys561-Lys887				
	KLC H3's	Lys561-Lys561							
	KLC-TPR(B) to Motor (B)	Lys393-Lys28	Lys393-Lys34	Lys495-Lys68	Lys495-Lys72				
	KLC-H3 to motor-B	Lys561-Lys68	Lys561-Lys99	Lys561-Lys142	Lys561-Lys188				
	KLC-TPR-B to CC4	Lys270-Lys877	Lys272-Lys877	Lys382-Lys911	Lys468-Lys905	Lys518-Lys884			
	KLC-TPR-B to Tail-B	Lys382-Lys957							
	KLC-TPR-A to CC4	Lys518-Lys846	Lys382-Lys846	Lys457-Lys846	Lys393-Lys803	Lys518-Lys815			
	KLC-TPR-A to CC1	Lys272-Lys465	Lys312-Lys465	Lys398-Lys465					

Figure S1

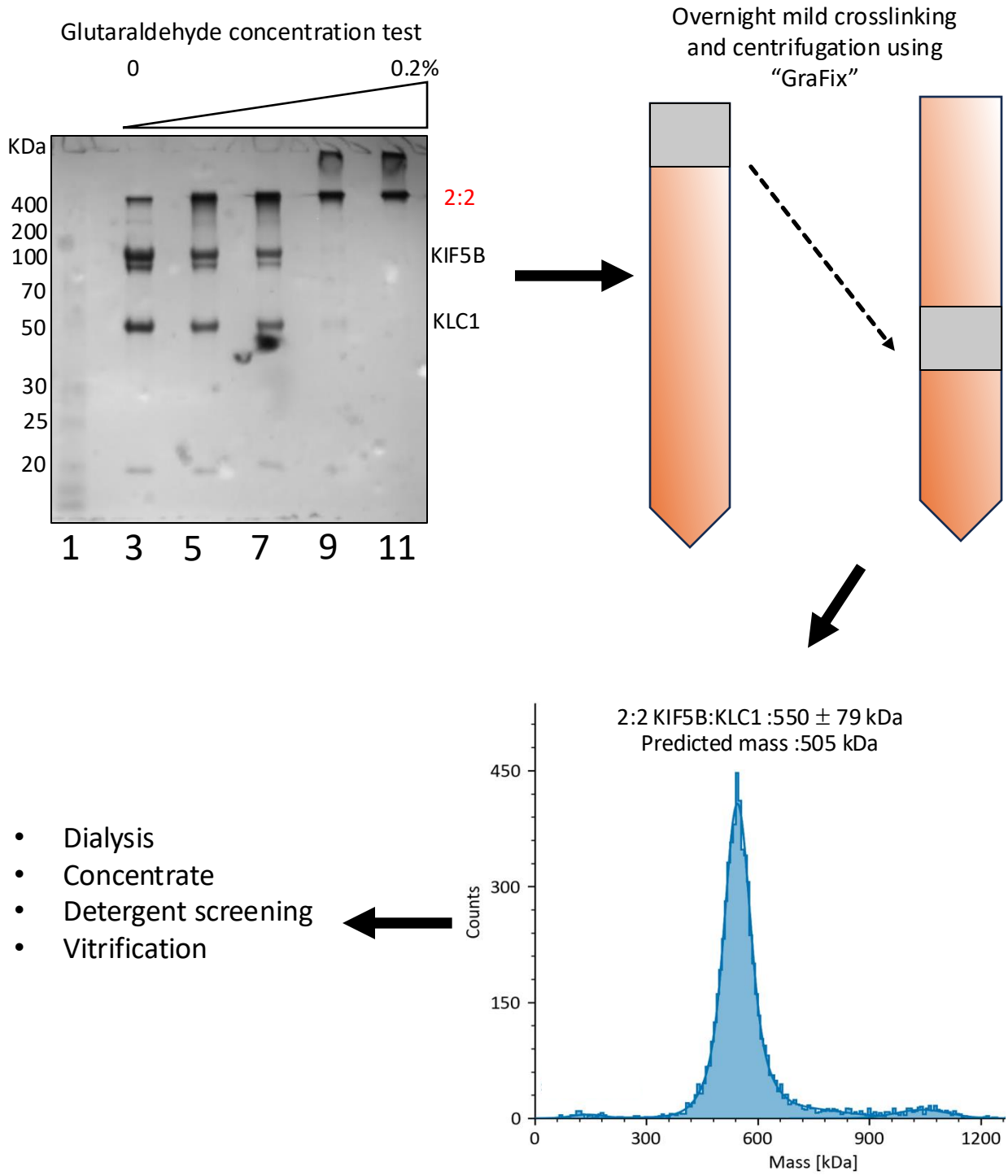
Glutaraldehyde concentration test
0
0.2%
KDa
400
200
100
70
50
30
25
20
2:2
KIF5B
KLC1
1
3
5
7
9
11
Overnight mild crosslinking and centrifugation using "GraFix"
2:2 KIF5B:KLC1 :550 ± 79 kDa
Predicted mass :505 kDa
Counts
450
300
150
0
0
300
600
900
1200
Mass [kDa]
Dialysis
Concentrate
Detergent screening
Vitrification

Figure S2

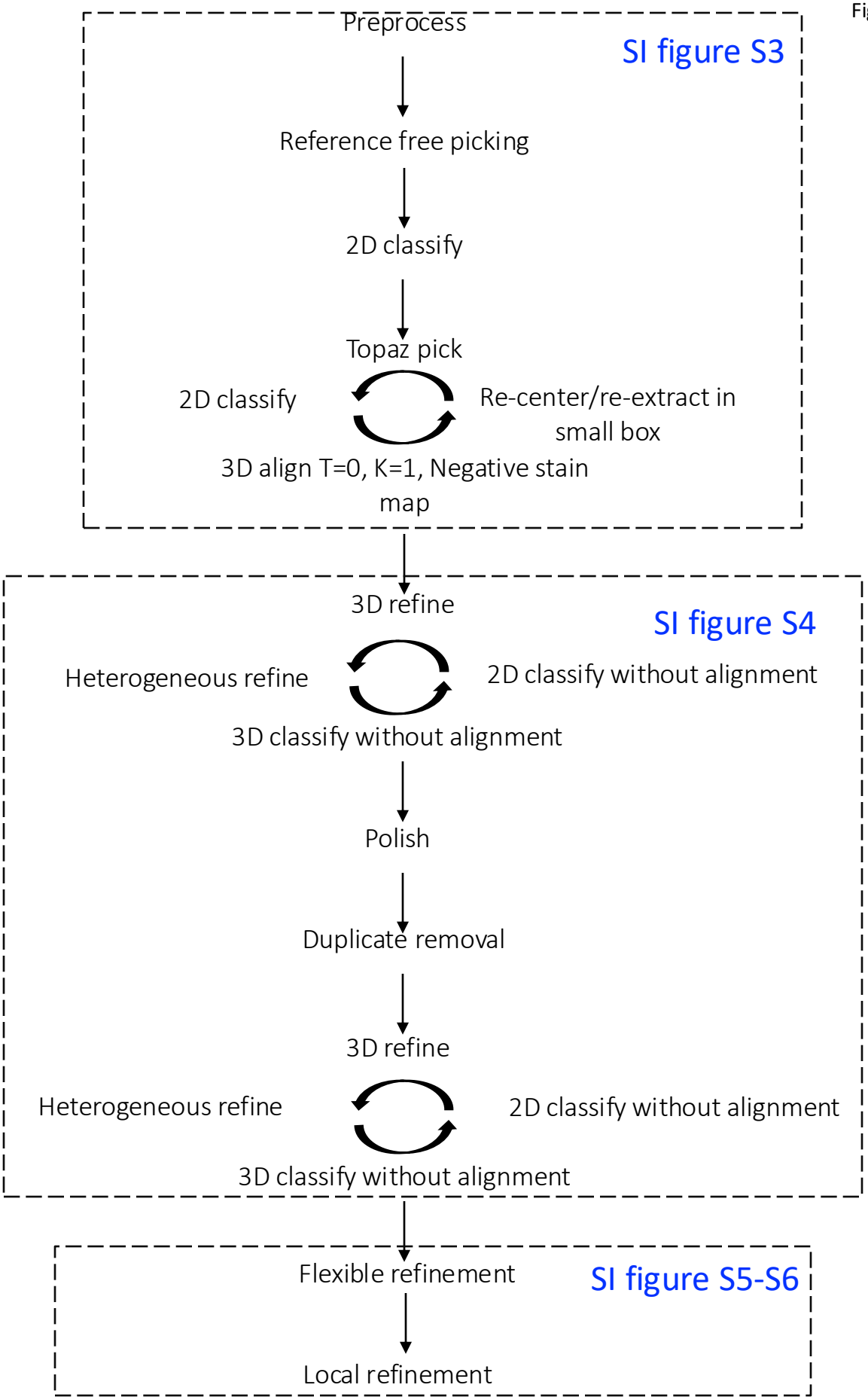
Preprocess
SI figure S3
Reference free picking
2D classify
Topaz pick
2D classify
Re-center/re-extract in small box
3D align T=0, K=1, Negative stain map
3D refine
SI figure S4
Heterogeneous refine
2D classify without alignment
3D classify without alignment
Polish
Duplicate removal
3D refine
Heterogeneous refine
2D classify without alignment
3D classify without alignment
Flexible refinement
SI figure S5-S6
Local refinement

Figure S3

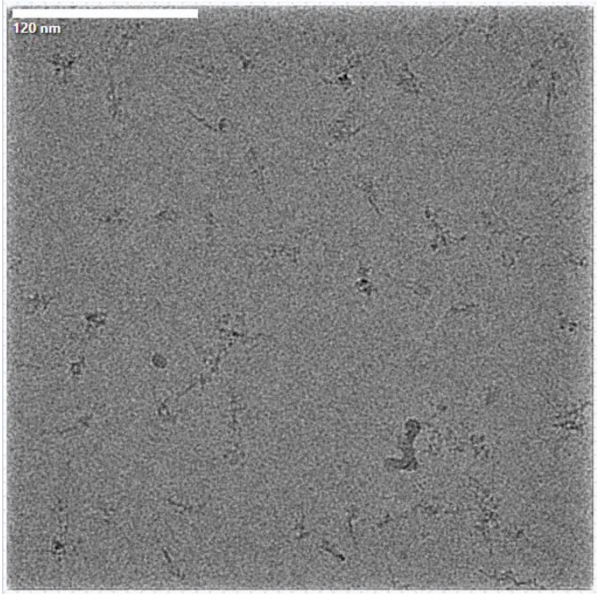

4 Datasets

- Preprocessing
- autopick

2D classify

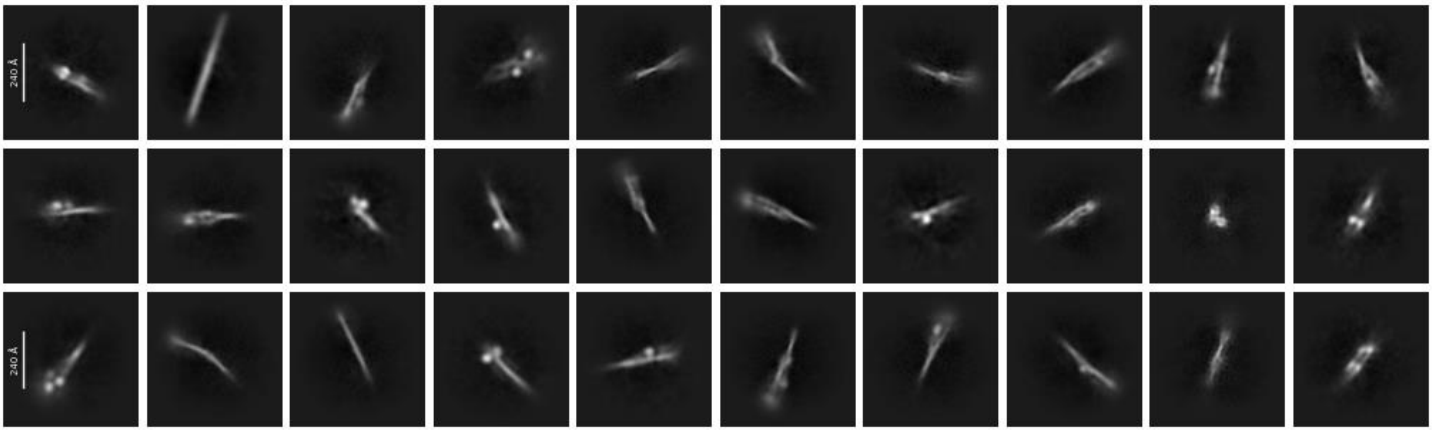

3D align T=0, K=1, using Negative stain map (tan et al 2023)

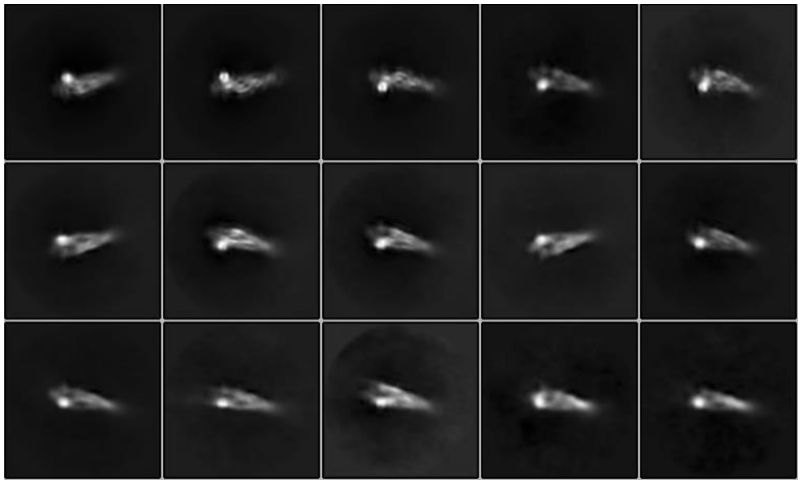

3D refine

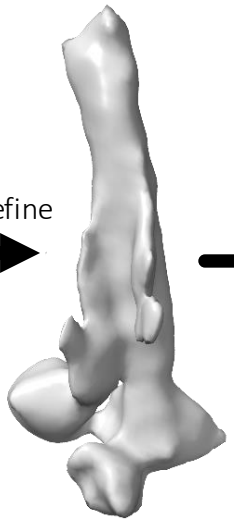

- 3D- and 2D-classification
- Improved picking/centering

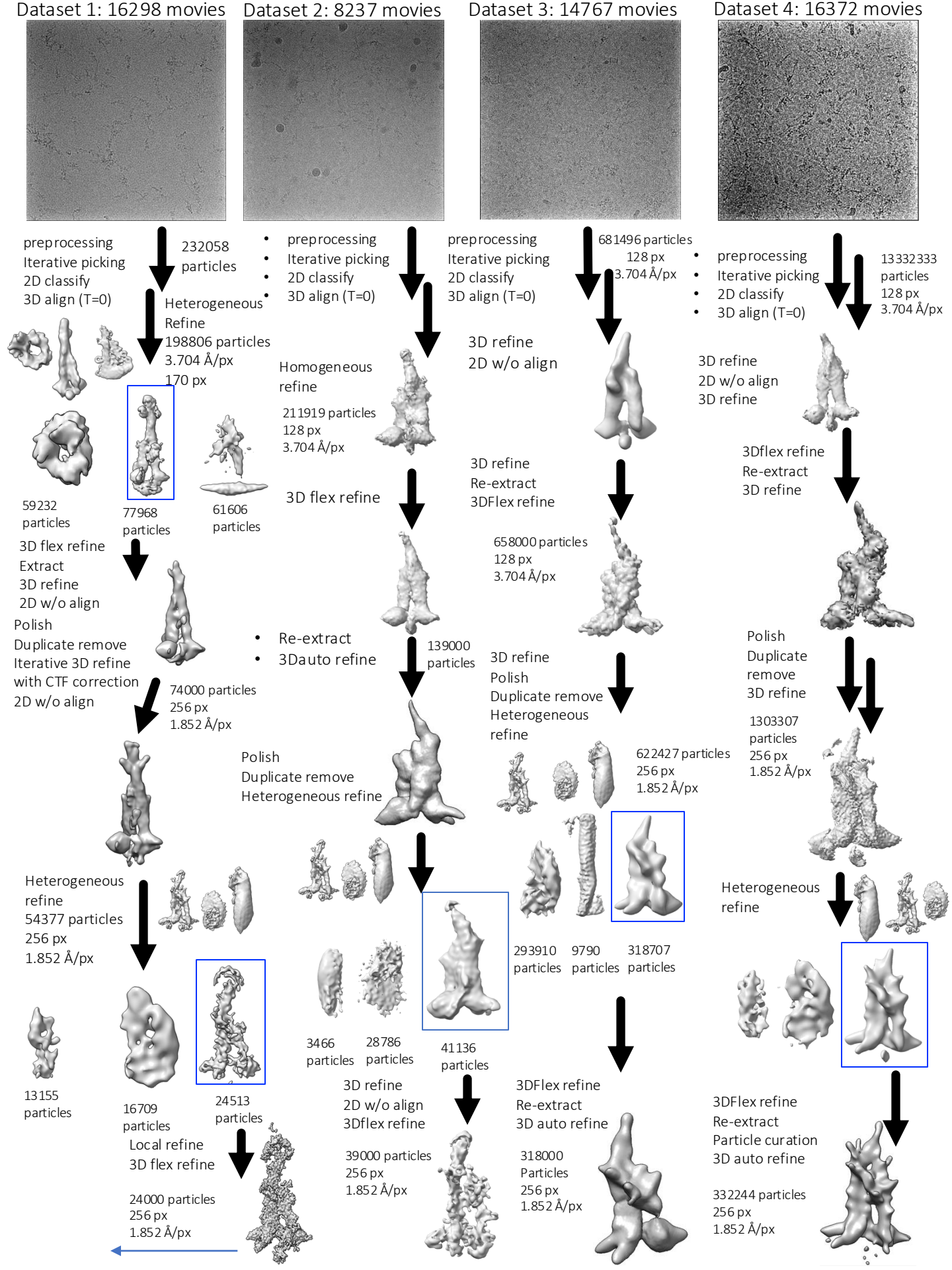
Dataset 1: 16298 movies
Dataset 2: 8237 movies
Dataset 3: 14767 movies
Dataset 4: 16372 movies
preprocessing
Iterative picking
2D classify
3D align (T=0)
232058 particles
Heterogeneous Refine
198806 particles
3.704 Å/px
170 px
59232 particles
77968 particles
61606 particles
3D flex refine
Extract
3D refine
2D w/o align
Polish
Duplicate remove
Iterative 3D refine
with CTF correction
2D w/o align
74000 particles
256 px
1.852 Å/px
Heterogeneous refine
54377 particles
256 px
1.852 Å/px
13155 particles
16709 particles
24513 particles
Local refine
3D flex refine
24000 particles
256 px
1.852 Å/px
preprocessing
Iterative picking
2D classify
3D align (T=0)
Homogeneous refine
211919 particles
128 px
3.704 Å/px
3D flex refine
Re-extract
3Dauto refine
139000 particles
Polish
Duplicate remove
Heterogeneous refine
3466 particles
28786 particles
41136 particles
3D refine
2D w/o align
3Dflex refine
39000 particles
256 px
1.852 Å/px
preprocessing
Iterative picking
2D classify
3D align (T=0)
681496 particles
128 px
3.704 Å/px
3D refine
2D w/o align
3D refine
Re-extract
3DFlex refine
658000 particles
128 px
3.704 Å/px
3D refine
Polish
Duplicate remove
Heterogeneous refine
622427 particles
256 px
1.852 Å/px
293910 particles
9790 particles
318707 particles
3DFlex refine
Re-extract
3D auto refine
318000 Particles
256 px
1.852 Å/px
preprocessing
Iterative picking
2D classify
3D align (T=0)
13332333 particles
128 px
3.704 Å/px
3D refine
2D w/o align
3D refine
3Dflex refine
Re-extract
3D refine
Polish
Duplicate remove
3D refine
1303307 particles
256 px
1.852 Å/px
Heterogeneous refine
3DFlex refine
Re-extract
Particle curation
3D auto refine
332244 particles
256 px
1.852 Å/px

Figure S5

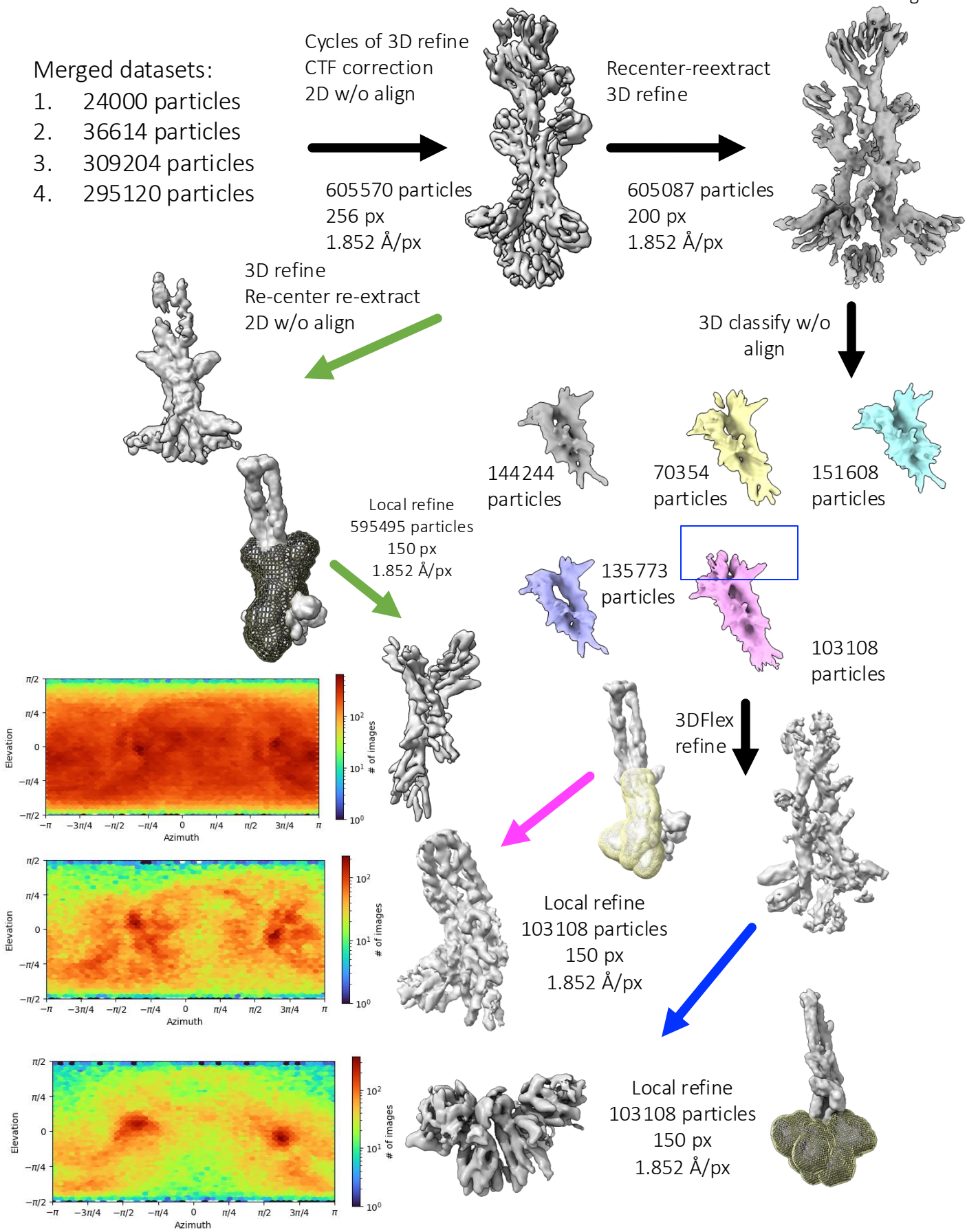
Merged datasets:
1. 24000 particles
2. 36614 particles
3. 309204 particles
4. 295120 particles
Cycles of 3D refine
CTF correction
2D w/o align
605570 particles
256 px
1.852 Å/px
Recenter-reextract
3D refine
605087 particles
200 px
1.852 Å/px
3D refine
Re-center re-extract
2D w/o align
3D classify w/o align
144244 particles
70354 particles
151608 particles
Local refine
595495 particles
150 px
1.852 Å/px
135773 particles
103108 particles
3DFlex refine
Local refine
103108 particles
150 px
1.852 Å/px
Local refine
103108 particles
150 px
1.852 Å/px
Elevation
Azimuth
# of images

Figure S6

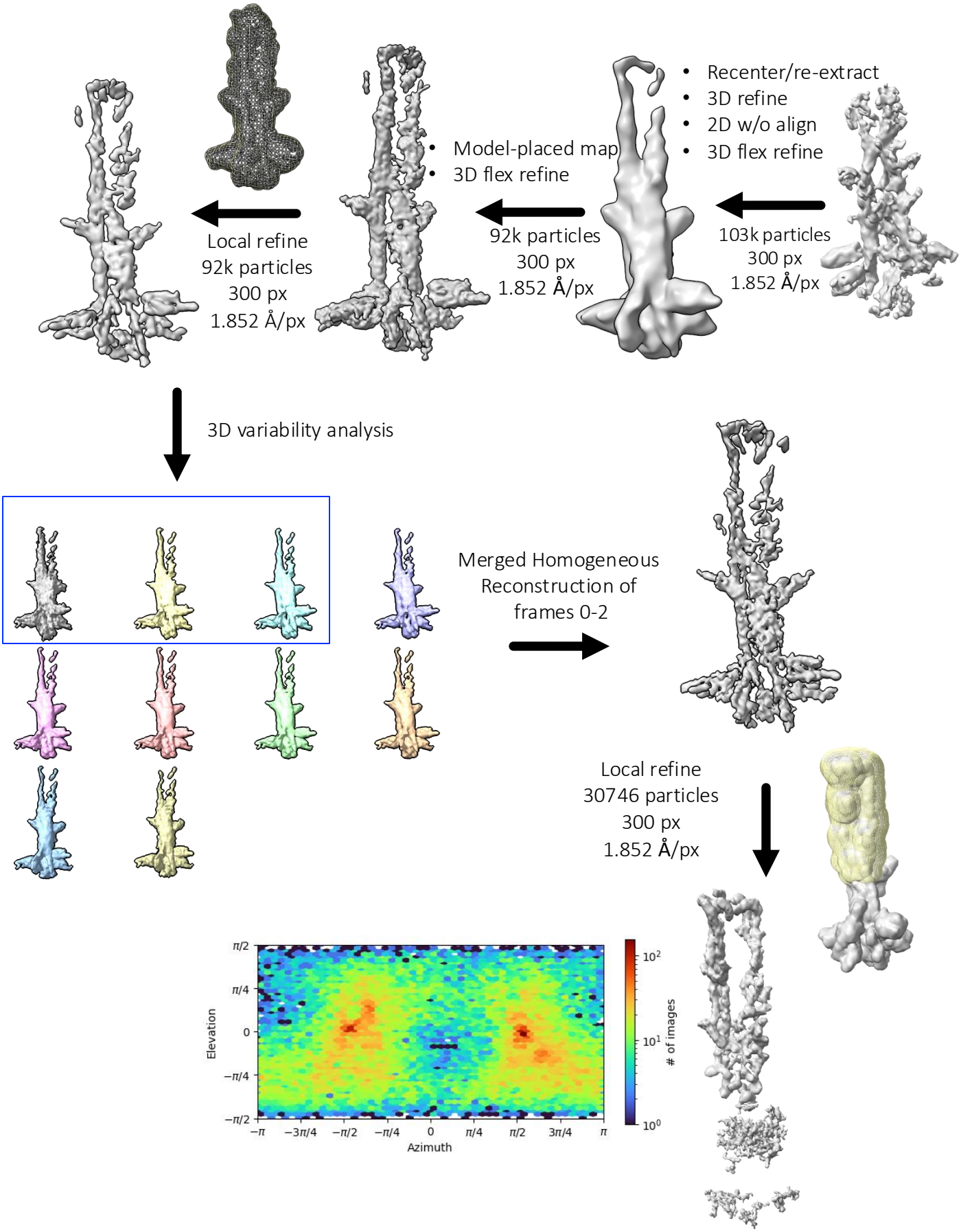
Recenter/re-extract
3D refine
2D w/o align
3D flex refine
103k particles
300 px
1.852 Å/px
Model-placed map
3D flex refine
92k particles
300 px
1.852 Å/px
Local refine
92k particles
300 px
1.852 Å/px
3D variability analysis
Merged Homogeneous Reconstruction of frames 0-2
Local refine
30746 particles
300 px
1.852 Å/px
Elevation
Azimuth
# of images

Figure S7

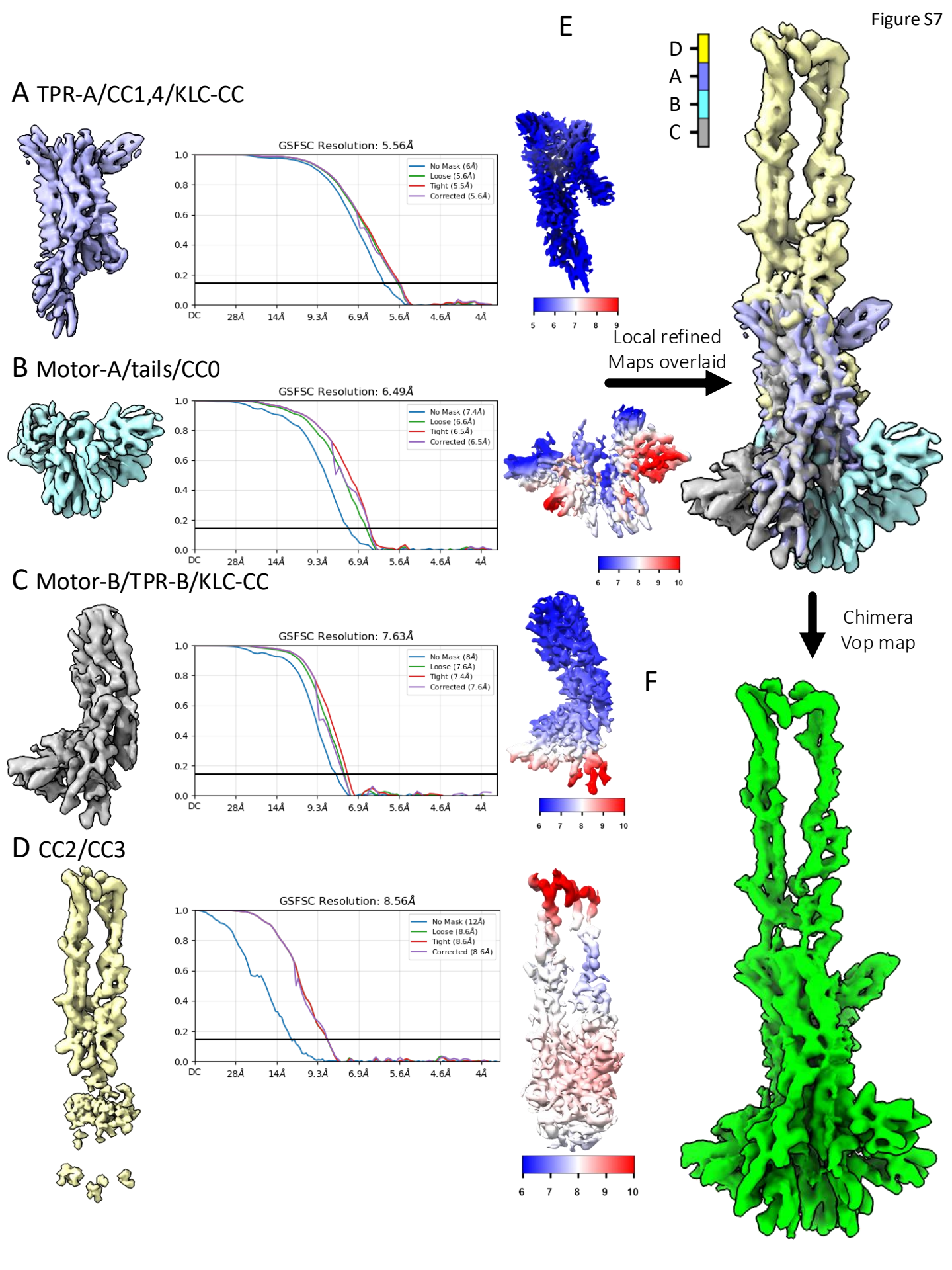
A TPR-A/CC1,4/KLC-CC
GSFSC Resolution: 5.56Å
No Mask (6Å)
Loose (5.6Å)
Tight (5.5Å)
Corrected (5.6Å)
B Motor-A/tails/CC0
GSFSC Resolution: 6.49Å
No Mask (7.4Å)
Loose (6.6Å)
Tight (6.5Å)
Corrected (6.5Å)
C Motor-B/TPR-B/KLC-CC
GSFSC Resolution: 7.63Å
No Mask (8Å)
Loose (7.6Å)
Tight (7.4Å)
Corrected (7.6Å)
D CC2/CC3
GSFSC Resolution: 8.56Å
No Mask (12Å)
Loose (8.6Å)
Tight (8.6Å)
Corrected (8.6Å)
E
D
A
B
C
Local refined
Maps overlaid
Chimera
Vop map
F

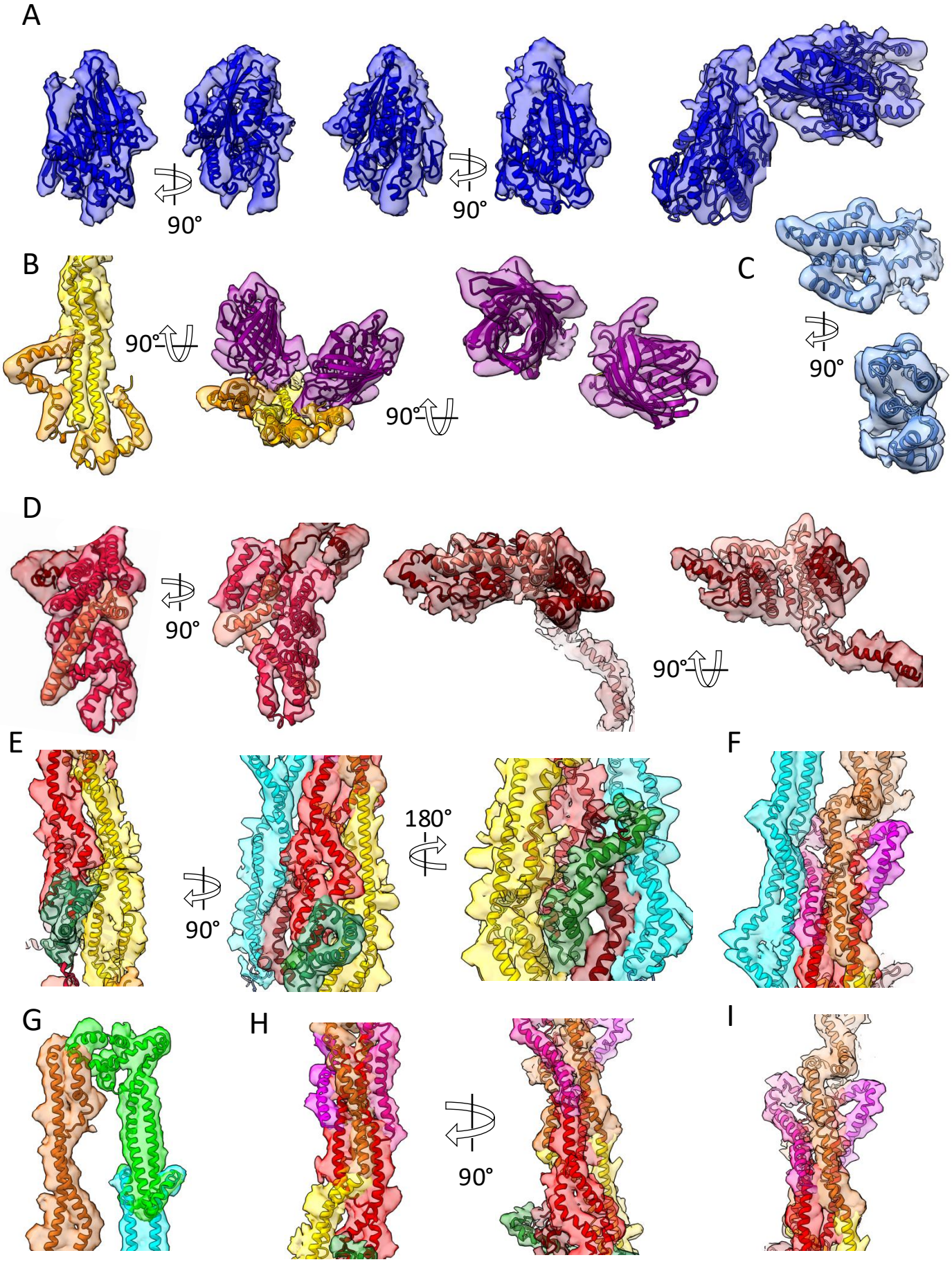
A
90°
90°
B
90°
90°
C
90°
D
90°
90°
E
90°
180°
F
G
H
90°
I

Figure S9

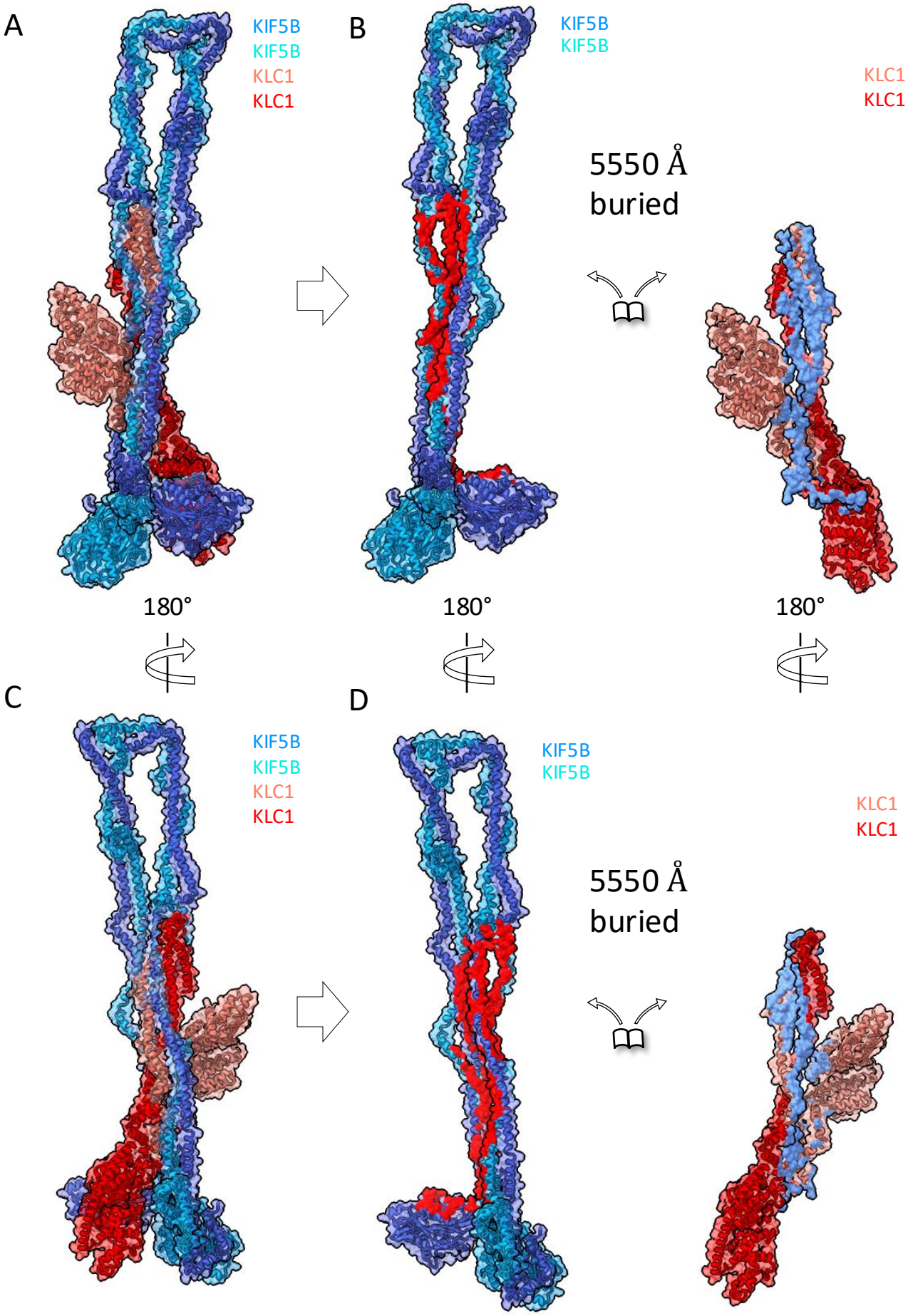
A
KIF5B
KIF5B
KLC1
KLC1
B
KIF5B
KIF5B
KLC1
KLC1
5550 Å
buried
180°
180°
180°
C
KIF5B
KIF5B
KLC1
KLC1
D
KIF5B
KIF5B
KLC1
KLC1
5550 Å
buried

Figure S10

Alphafold3 of kinesin (KIF5B-KLC1 tetramer)

A

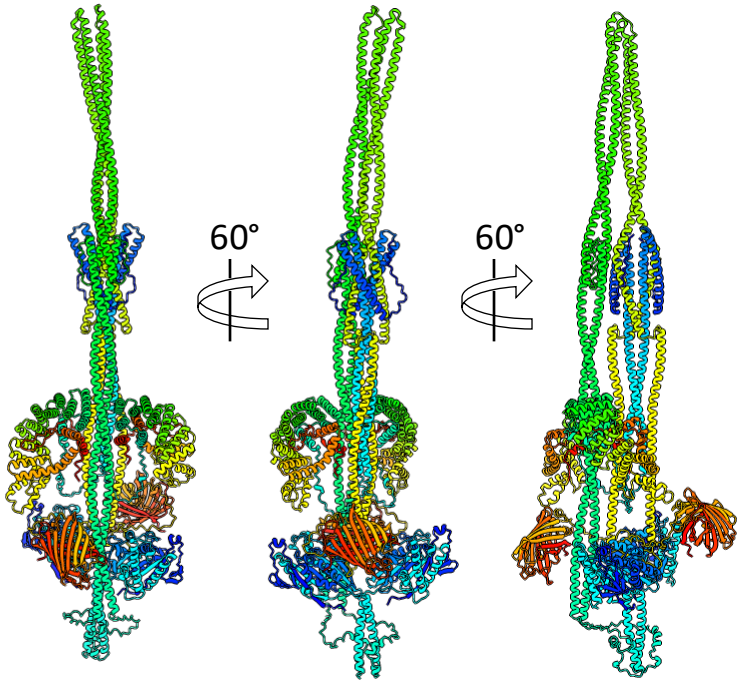

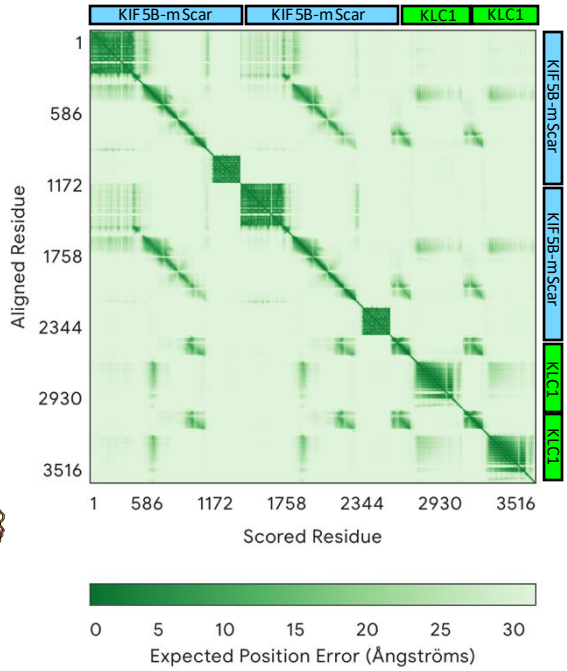

B

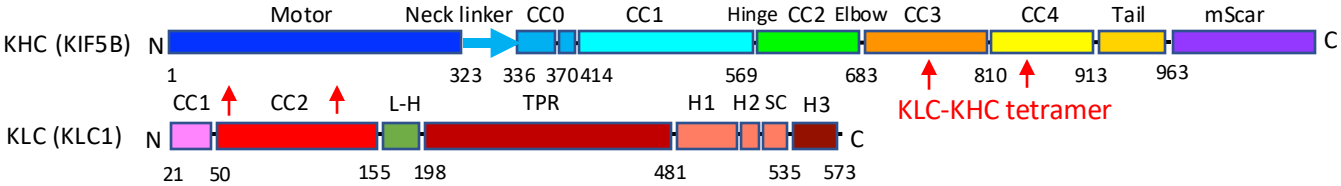

Cryo-EM model (this work)

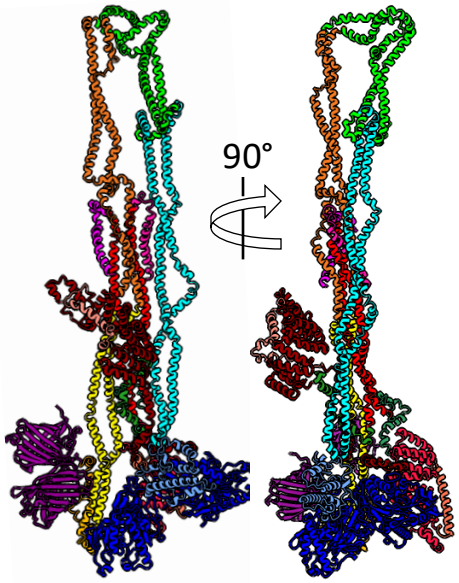

Alphafold3 predicted model

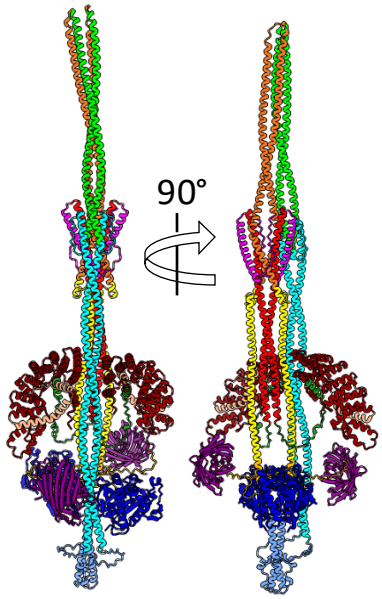

Negative stain model
(Tan & Cianfrocco et al)

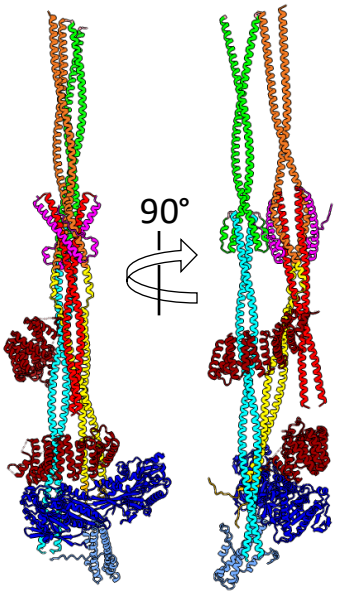

KIF5, KLC sequence conservation

Figure S11

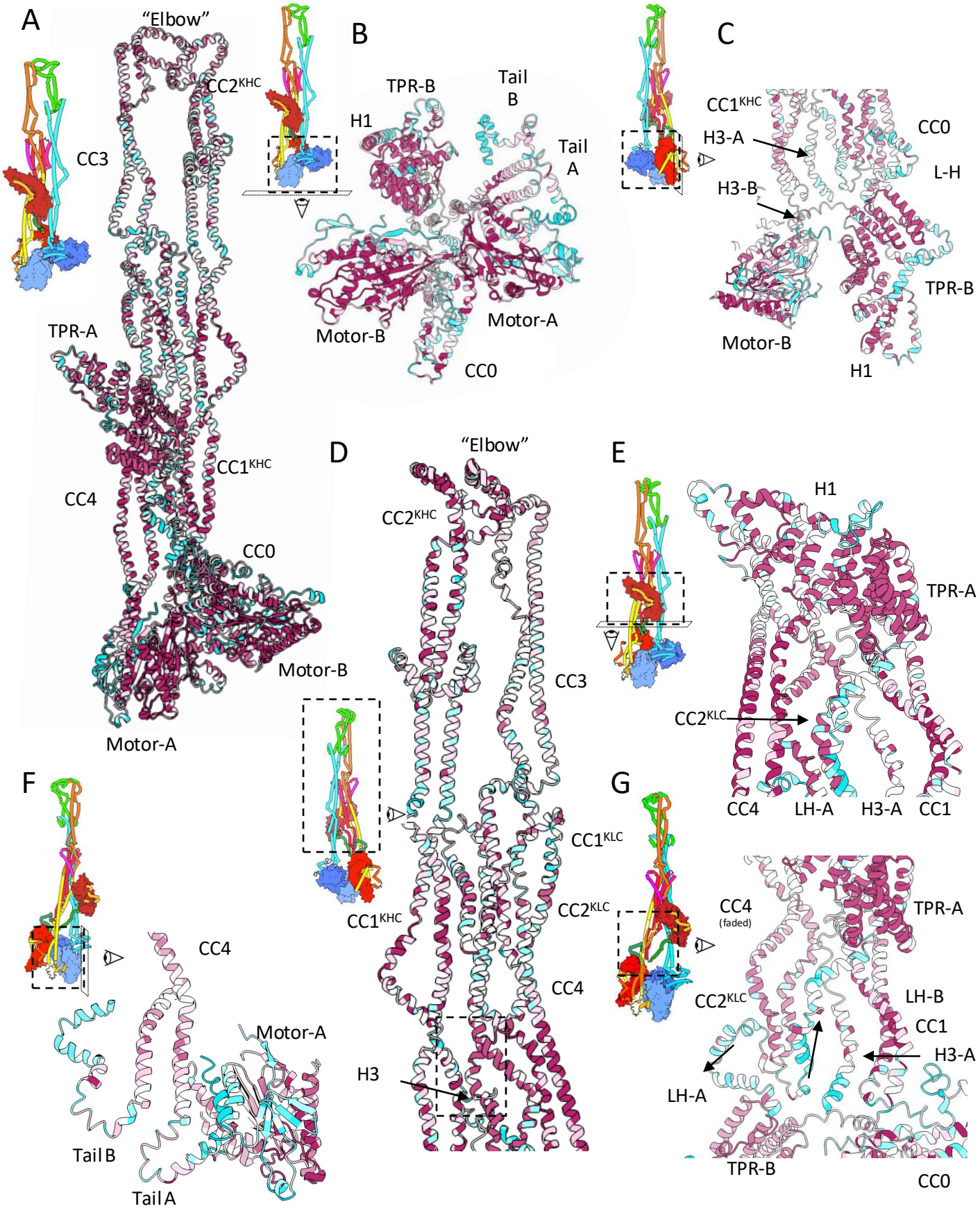

KIF5B-KLC1-XLMS (Tan et al 2023)

Figure S12

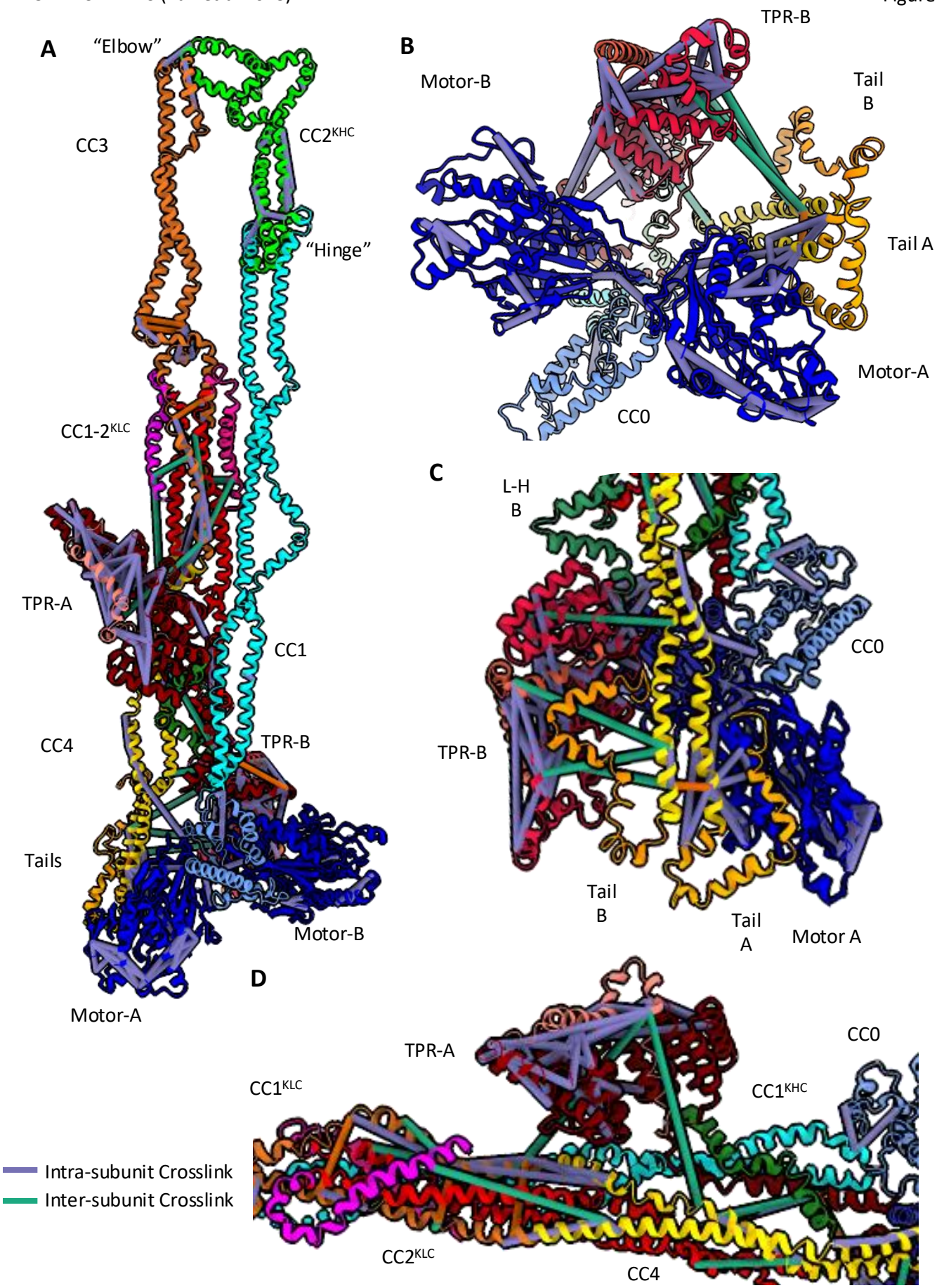

KIF5C-KLC1-XLMS (tan et al 2023)

Figure S13

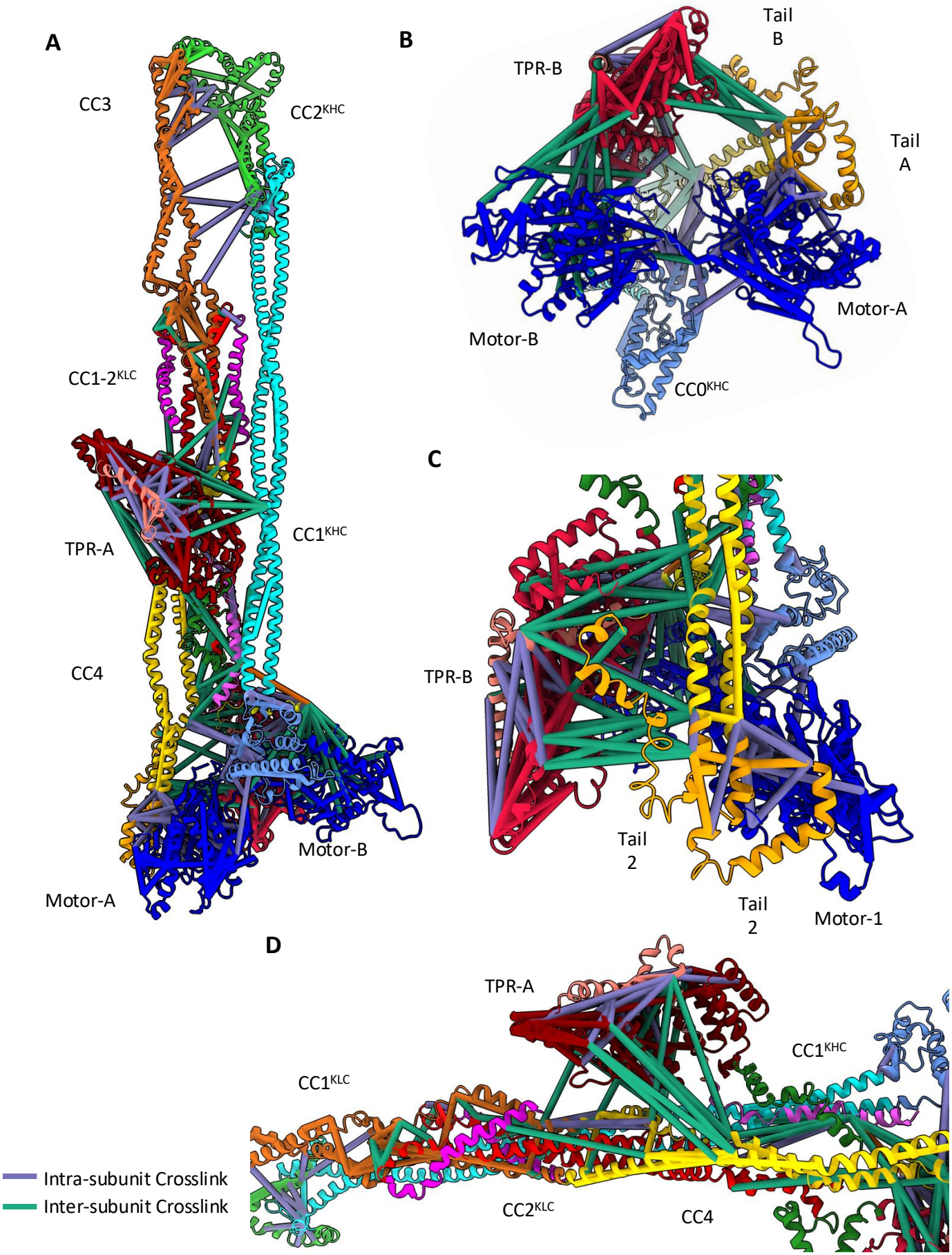

Figure S14

KIF5B KHC homodimer XLMS (Tan et al 2023)

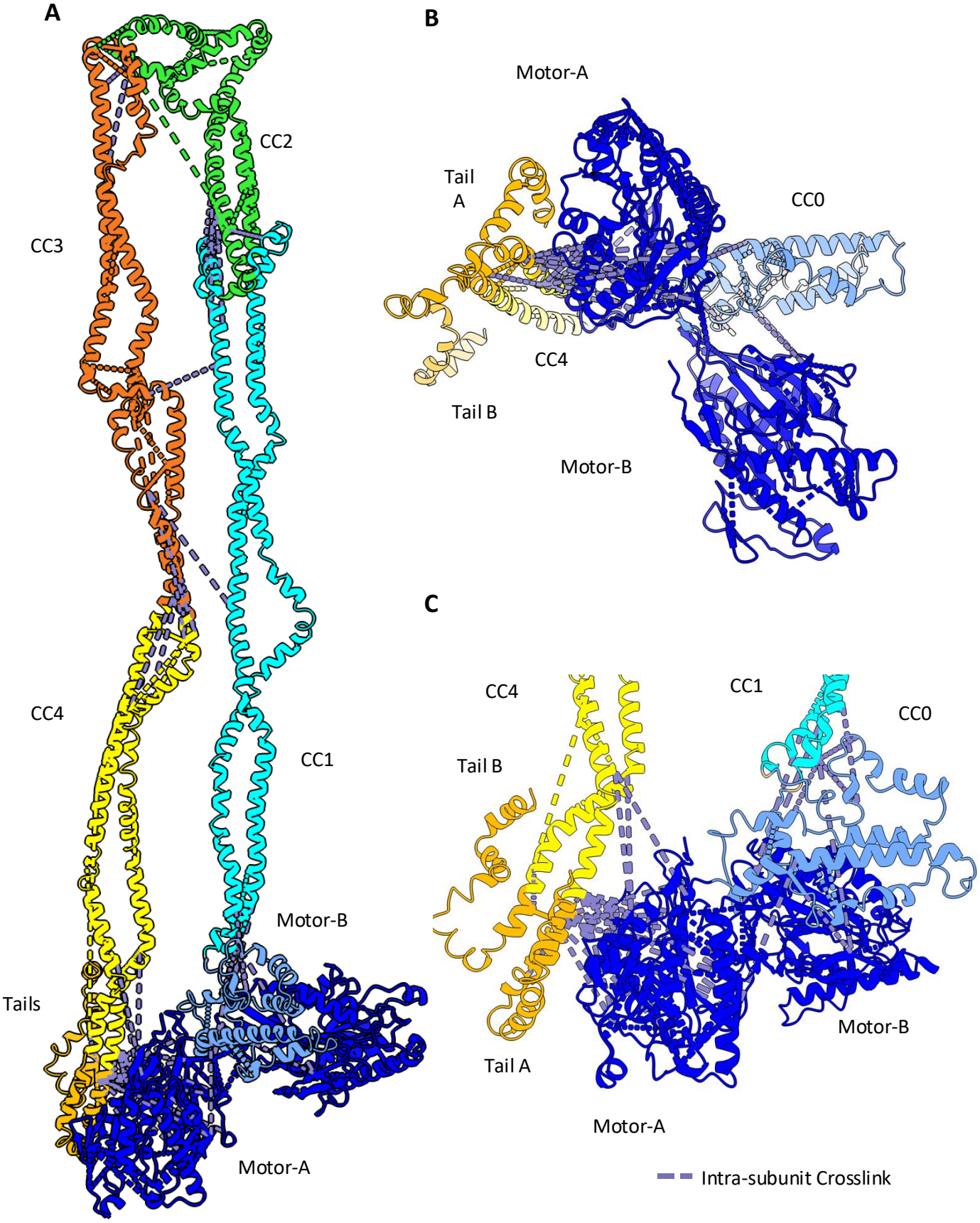

Figure S15

A

AlphaFold Model
MAP7D3 CTD (476-876)+ KHC KIF5B (1-587)

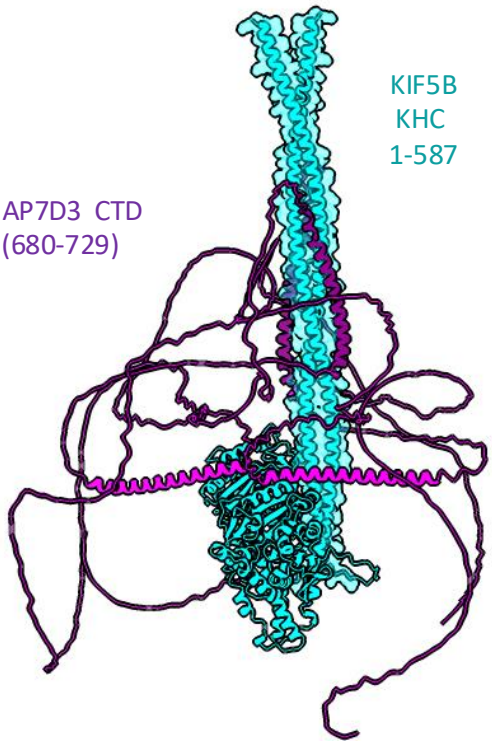

B

Trimmed Model
MAP7D3 (680-729)- KHC KIF5B CC (405-587)

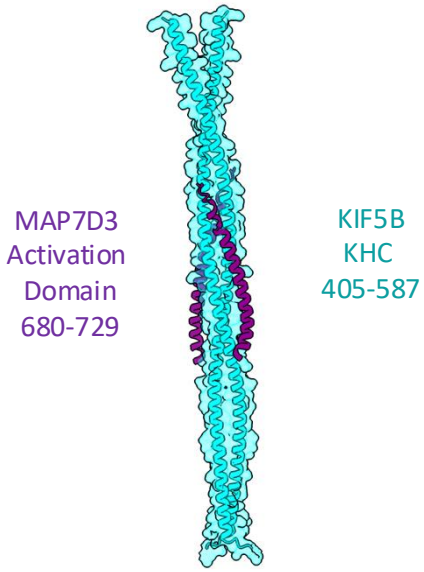

C

Model

Model + Kinesin-1 Overlay

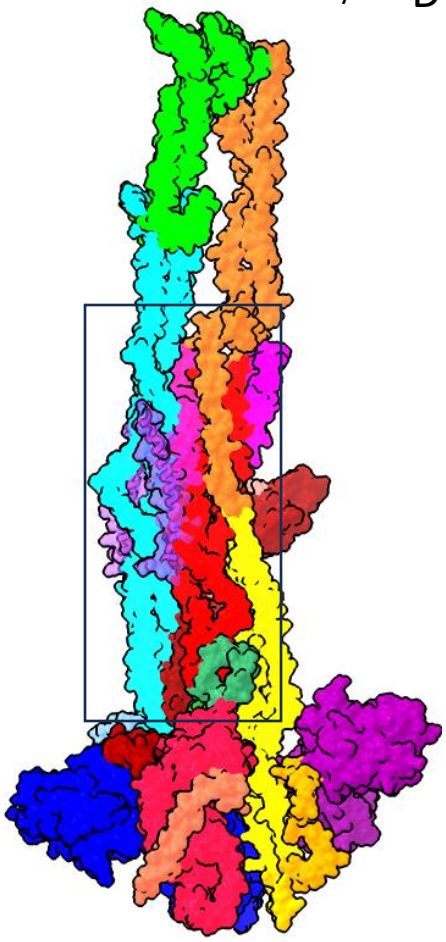

D

Close-up Model + Kinesin-1 Overlay

MAP7D3 sterically hinders
KHC CC3-CC4 binding onto CC1

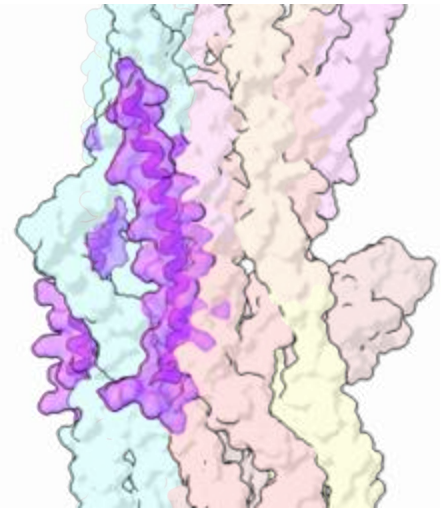

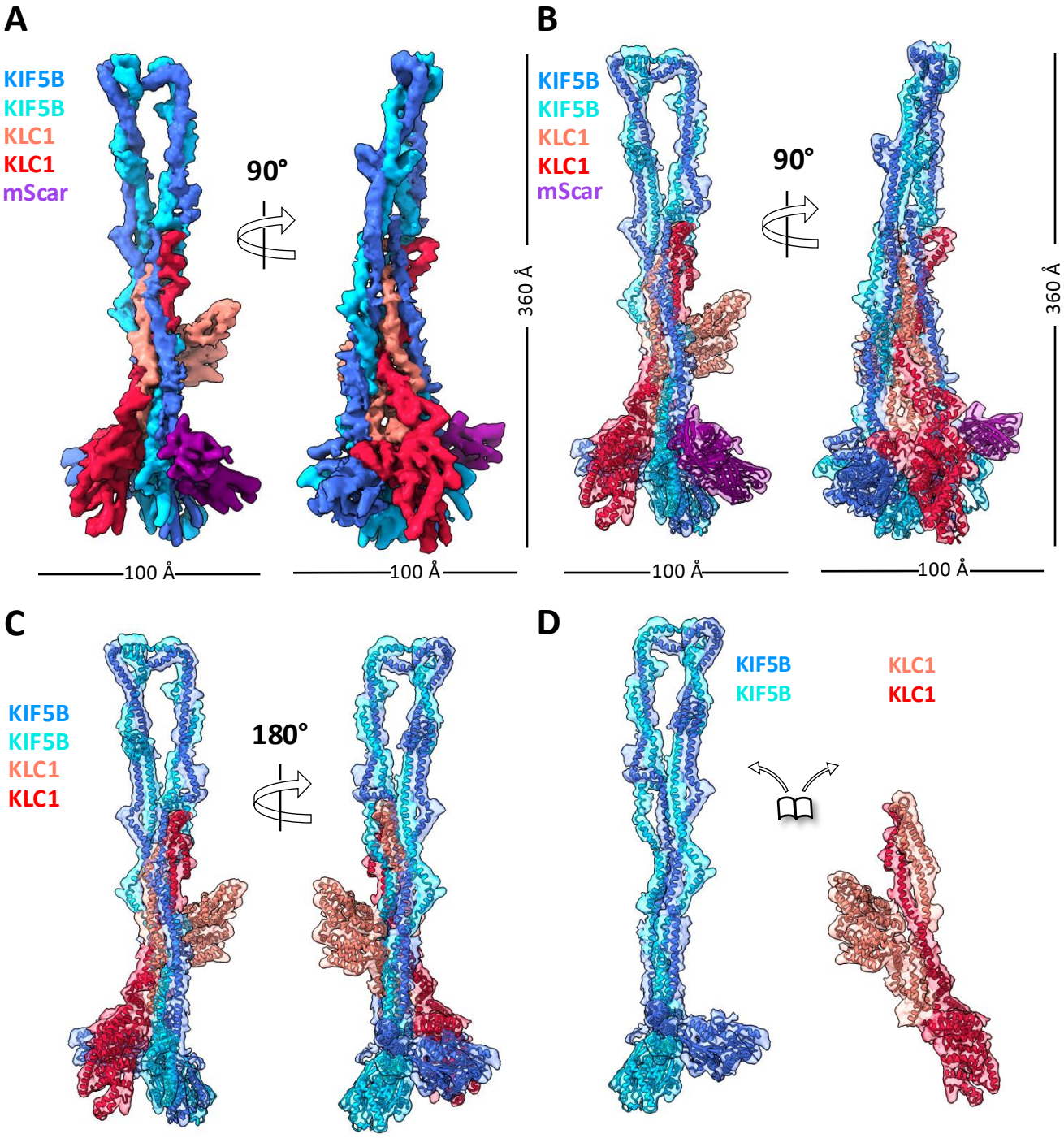
A
KIF5B
KIF5B
KLC1
KLC1
mScar
90°
360 Å
100 Å
100 Å
B
KIF5B
KIF5B
KLC1
KLC1
mScar
90°
360 Å
100 Å
100 Å
C
KIF5B
KIF5B
KLC1
KLC1
180°
D
KIF5B
KIF5B
KLC1
KLC1

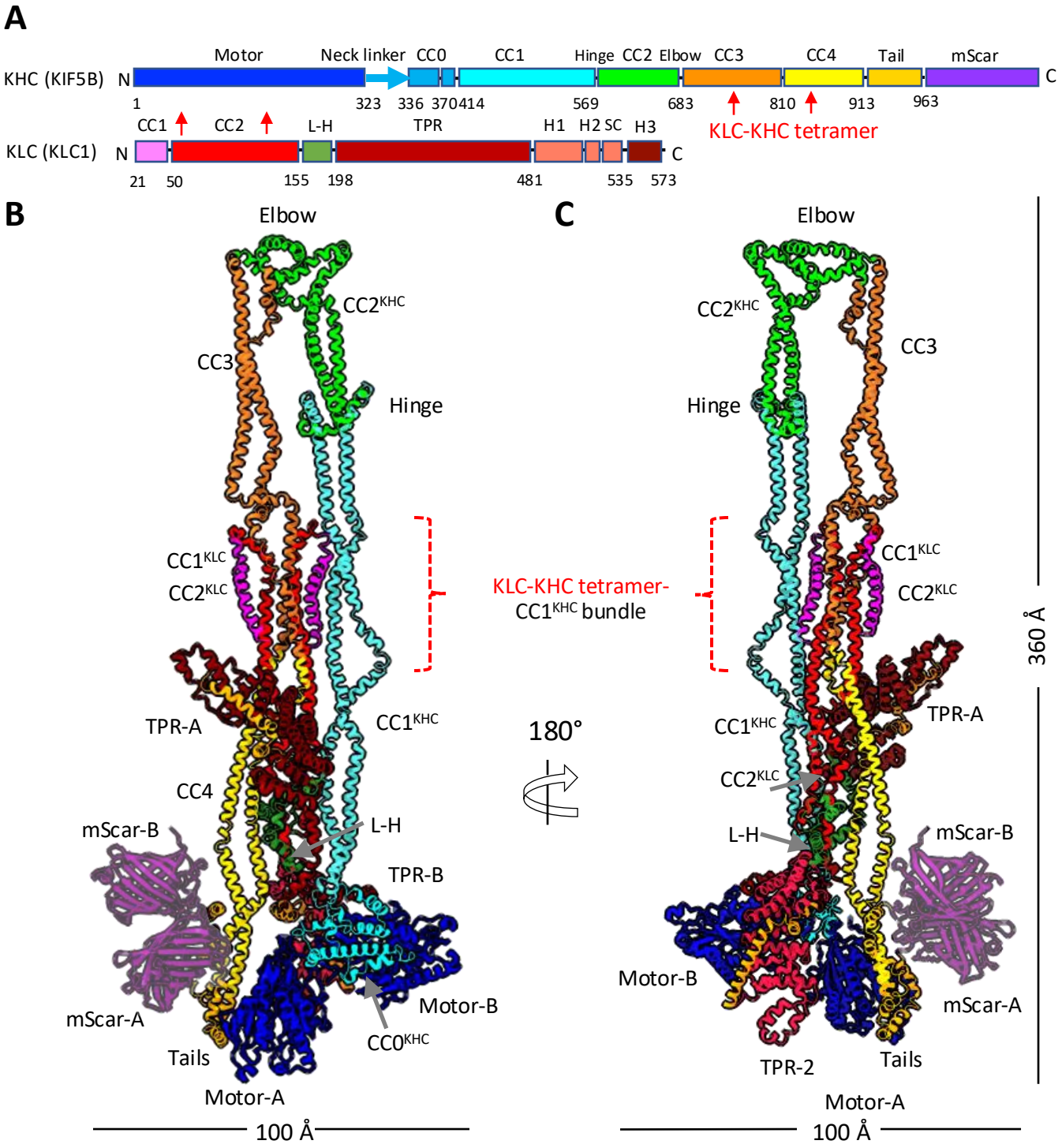
A
KHC (KIF5B)
N
C
Motor
Neck linker
CC0
CC1
Hinge
CC2
Elbow
CC3
CC4
Tail
mScar
1
323
336
370
414
569
683
810
913
963
KLC-KHC tetramer
KLC (KLC1)
CC1
CC2
L-H
TPR
H1
H2
SC
H3
21
50
155
198
481
535
573
B
Elbow
CC2KHC
CC3
Hinge
CC1KLC
CC2KLC
TPR-A
CC1KHC
CC4
L-H
mScar-B
TPR-B
mScar-A
Motor-B
CC0KHC
Tails
Motor-A
100 Å
KLC-KHC tetramer-
CC1KHC bundle
180°
C
Elbow
CC2KHC
CC3
Hinge
CC1KLC
CC2KLC
TPR-A
CC1KHC
CC2KLC
L-H
mScar-B
Motor-B
mScar-A
TPR-2
Tails
Motor-A
100 Å
360 Å

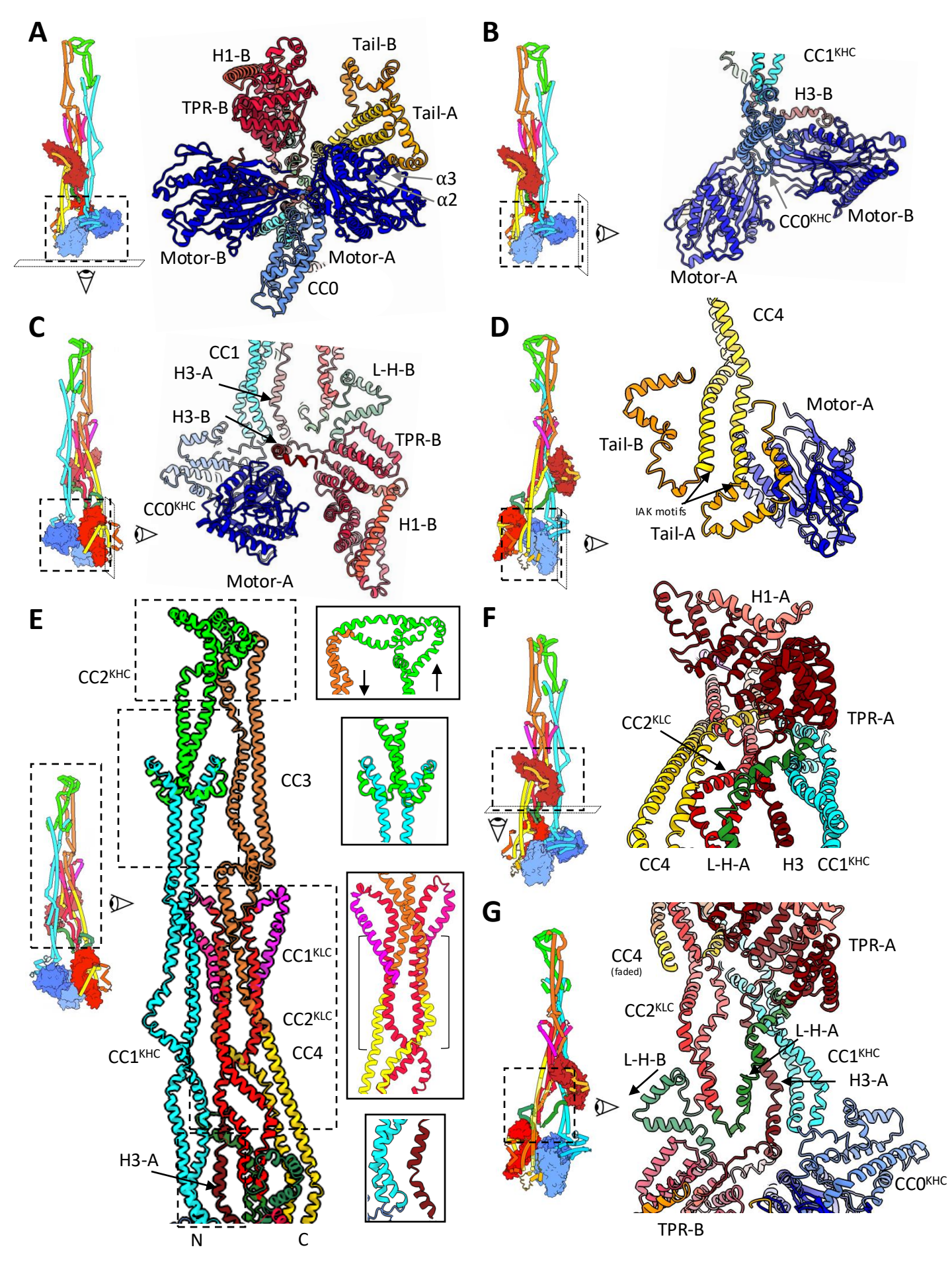
A
H1-B
Tail-B
TPR-B
Tail-A
α3
α2
Motor-B
Motor-A
CC0
B
CC1KHC
H3-B
CC0KHC
Motor-B
Motor-A
C
CC1
H3-A
L-H-B
H3-B
TPR-B
CC0KHC
H1-B
Motor-A
D
CC4
Motor-A
Tail-B
IAK motifs
Tail-A
E
CC2KHC
CC3
CC1KLC
CC2KLC
CC4
CC1KHC
H3-A
N
C
F
H1-A
CC2KLC
TPR-A
CC4
L-H-A
H3
CC1KHC
G
CC4
(faded)
TPR-A
CC2KLC
L-H-A
L-H-B
CC1KHC
H3-A
CC0KHC
TPR-B

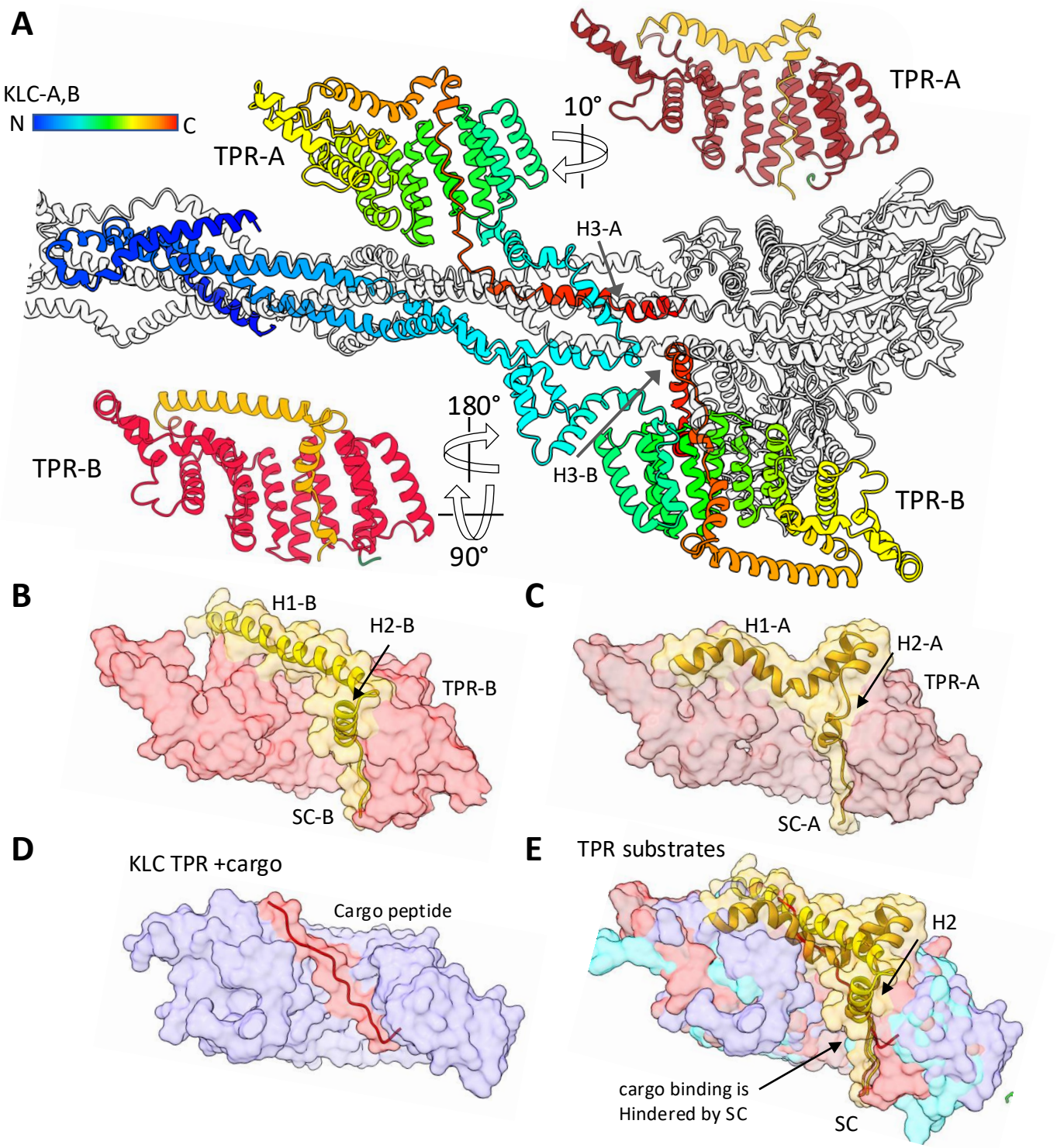
A
KLC-A,B
N
C
TPR-A
10°
TPR-A
H3-A
180°
TPR-B
H3-B
TPR-B
90°
B
H1-B
H2-B
TPR-B
SC-B
C
H1-A
H2-A
TPR-A
SC-A
D
KLC TPR +cargo
Cargo peptide
E
TPR substrates
H2
cargo binding is
Hindered by SC
SC

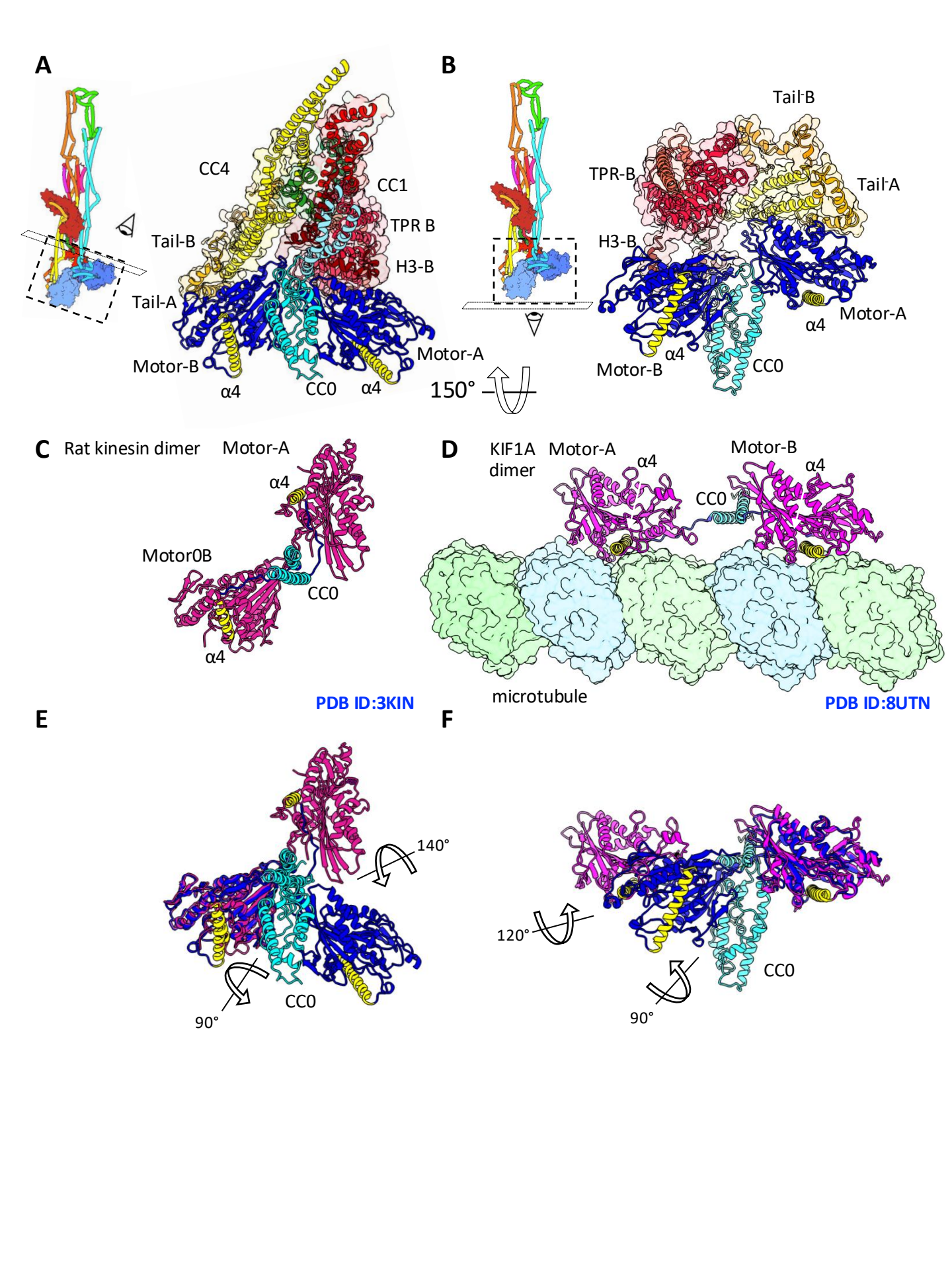
A
CC4
CC1
TPR B
Tail-B
H3-B
Tail-A
Motor-B
α4
CC0
α4
Motor-A
150°
B
Tail-B
TPR-B
Tail-A
H3-B
Motor-A
α4
α4
Motor-B
CC0
C
Rat kinesin dimer
Motor-A
α4
Motor0B
CC0
α4
PDB ID:3KIN
D
KIF1A dimer
Motor-A
α4
Motor-B
α4
CC0
microtubule
PDB ID:8UTN
E
140°
90°
CC0
F
120°
90°
CC0

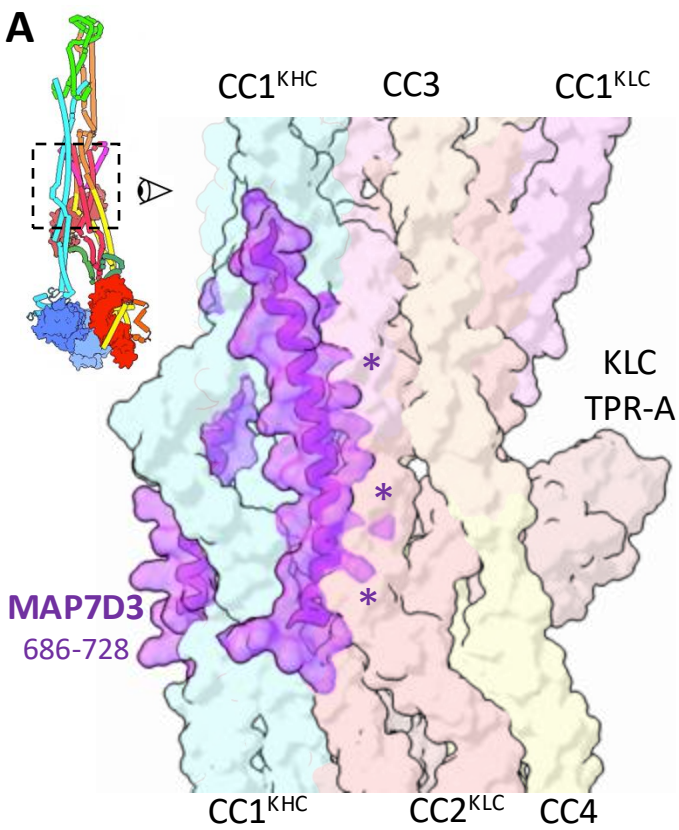
A
CC1KHC
CC3
CC1KLC
KLC
TPR-A
MAP7D3
686-728
CC1KHC
CC2KLC
CC4

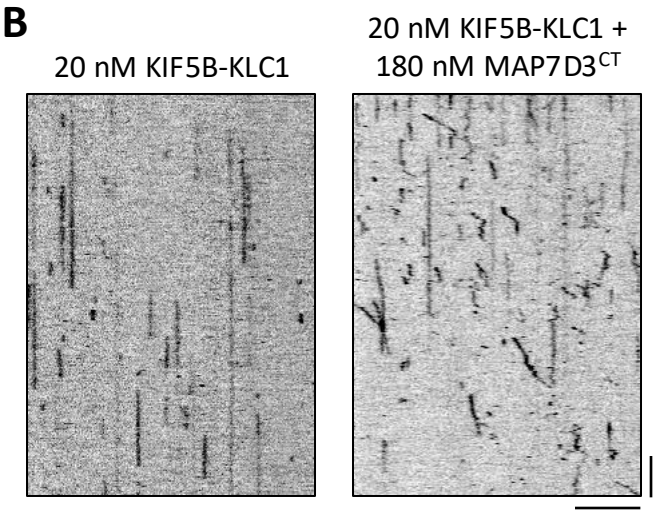
B
20 nM KIF5B-KLC1
20 nM KIF5B-KLC1 +
180 nM MAP7D3CT

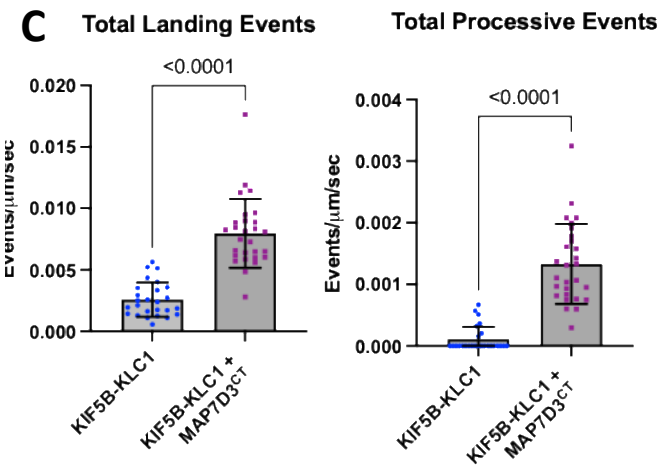
C
Total Landing Events
Total Processive Events
<0.0001
<0.0001
Events/µm/sec
0.020
0.015
0.010
0.005
0.000
0.004
0.003
0.002
0.001
0.000
KIF5B-KLC1
KIF5B-KLC1 + MAP7D3CT

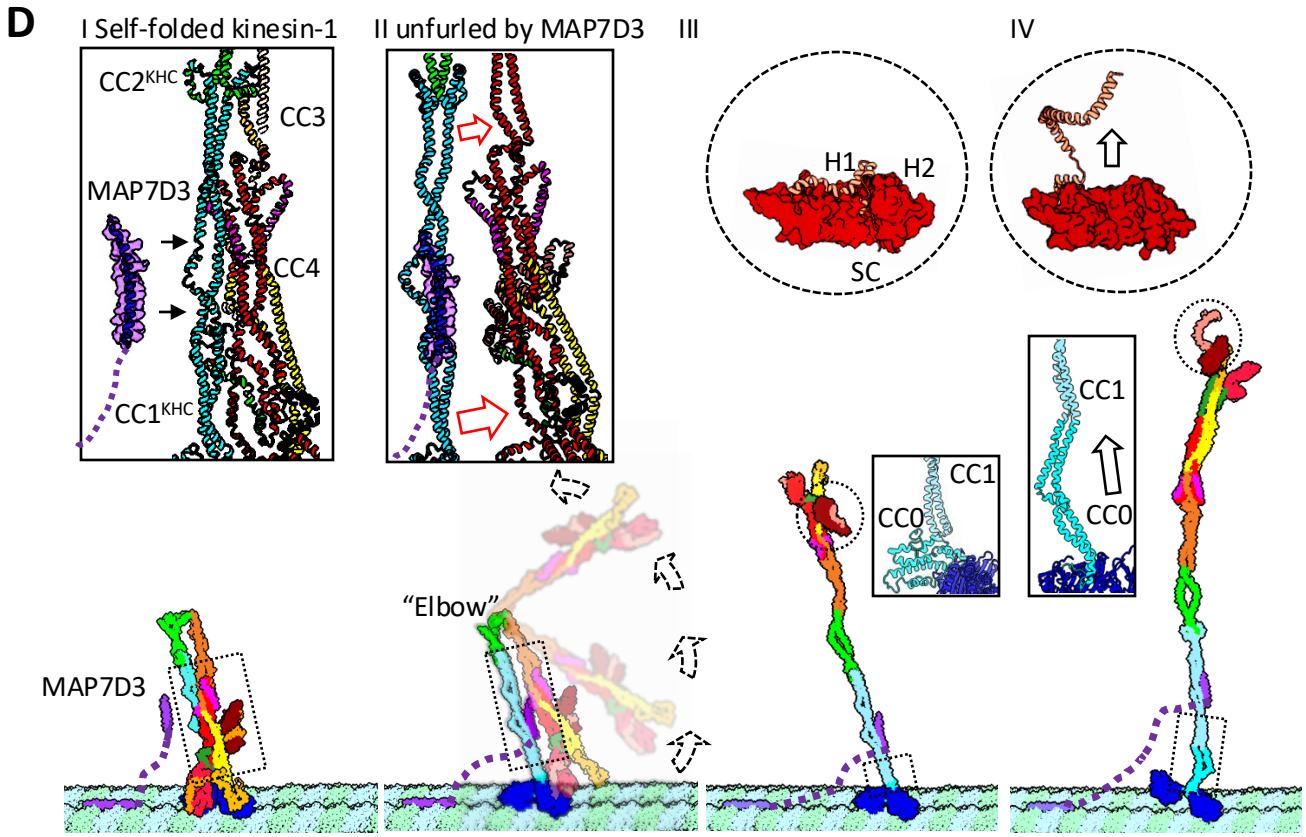
D
I Self-folded kinesin-1
II unfurled by MAP7D3
III
IV
CC2KHC
CC3
MAP7D3
CC4
CC1KHC
H1
H2
SC
CC1
CC0
CC1
CC0
"Elbow"
MAP7D3